Zebrafish models of human-duplicated *SRGAP2* reveal novel functions in microglia and visual system development

Authors:
José M. Uribe-Salazar[1†], Gulhan Kaya[1], KaeChandra Weyenberg[1], Brittany Radke[1], Keiko Hino[2], Daniela C. Soto[1], Jia-Lin Shiu[2], Wenzhu Zhang[2], Cole Ingamells[1], Nicholas K. Haghani[1], Emily Xu[1], Joseph Rosas[2], Sergi Simó[2], Joel Miesfeld[3], Tom Glaser[2], Scott C. Baraban[4], Li-En Jao[2], Megan Y. Dennis[1†]

[1]Genome Center, MIND Institute, and Department of Biochemistry & Molecular Medicine, University of California, Davis, CA, USA
[2]Department of Cell Biology and Human Anatomy, University of California, Davis, CA, USA
[3]Department of Ophthalmology and Visual Sciences, Medical College of Wisconsin, WI, USA
[4]Department of Neurological Surgery and Weill Institute for Neurosciences, University of California, San Francisco, CA, USA

[†]Corresponding author:
Megan Y. Dennis, Ph.D.
University of California, Davis, School of Medicine
One Shields Avenue
Genome Center, 4303 GBSF
Davis, CA 95616
Email: mydennis@ucdavis.edu

Keywords: gene duplication, human evolution, zebrafish, *Danio rerio*, brain development, eye development, microglia

Abstract

The expansion of the human *SRGAP2* family, resulting in a human-specific paralog *SRGAP2C,* likely contributed to altered evolutionary brain features. The introduction of *SRGAP2C* in mouse models is associated with changes in cortical neuronal migration, axon guidance, synaptogenesis, and sensory-task performance. Truncated SRGAP2C heterodimerizes with the full-length ancestral gene product SRGAP2A and antagonizes its functions. However, the significance of *SRGAP2* duplication beyond neocortex development has not been elucidated due to the embryonic lethality of complete *Srgap2* knockout in mice. Using zebrafish, we show that *srgap2* knockout results in viable offspring and that these larvae phenocopy "humanized" *SRGAP2C* larvae, including altered morphometric features (i.e., reduced body length and inter-eye distance) and differential expression of synapse-, axonogenesis-, and vision-related genes. Through single-cell transcriptome analysis, we demonstrate a skewed balance of excitatory and inhibitory neurons that likely contribute to increased susceptibility to seizures displayed by *Srgap2* mutant larvae, a phenotype resembling *SRGAP2* loss-of-function in a child with early infantile epileptic encephalopathy. Single-cell data also shows strong endogenous expression of *srgap2* in microglia with mutants exhibiting altered membrane dynamics and likely delayed maturation of microglial cells. Microglia cells expressing *srgap2* were also detected in the developing eye together with altered expression of genes related to axonogenesis in mutant retinal cells. Consistent with the perturbed gene expression in the retina, we found that *SRGAP2* mutant larvae exhibited increased sensitivity to broad and fine visual cues. Finally, comparing the transcriptomes of relevant cell types between human (+*SRGAP2C*) and non-human primates (–*SRGAP2C*) revealed significant overlaps of gene alterations with mutant cells in our zebrafish models; this suggests that *SRGAP2C* plays a similar role altering microglia and the visual system in modern humans. Together, our functional characterization of conserved ortholog Srgap2 and human SRGAP2C in zebrafish uncovered novel gene functions and highlights the strength of cross-species analysis in understanding the development of human-specific features.

Abstract (short)

SRGAP2C has been implicated in contributing to altered brain features in the evolution of humans. However, the significance of *SRGAP2* duplication beyond neocortex development has not been elucidated due to the embryonic lethality of complete *Srgap2* knockout in mice. Using zebrafish, we show that *srgap2* knockout results in viable offspring that phenocopy "humanized" *SRGAP2C* larvae. Morphometric, behavioral, and transcriptome analyses collectively suggest *srgap2* impacts axonal guidance, synaptogenesis, and seizure susceptibility. Beyond neurons, *Srgap2* functions in controlling membrane dynamics and maturation of microglial cells, possibly leading to altered axonogenesis in the developing retina and increased sensitivity to broad and fine visual cues. Comparing relevant transcriptomes between human and nonhuman primates suggests that *SRGAP2C* similarly impacts microglia and vision in modern humans. Our functional characterization of conserved ortholog Srgap2 and human SRGAP2C in zebrafish uncovered novel gene functions and highlights the strength of cross-species analysis in understanding the development of human-specific features.

Introduction

Genetic factors contributing to phenotypic differences between humans and non-human primates remain largely undiscovered [1,2]. However, gene expansions [3,4] have been suggested as an important driver of primate species divergence [5–13], with mammalian and organoid models recapitulating hallmark features of human brain development, including altered synaptogenesis, corticogenesis, and gyrification [14–20]. One of the most well-studied human duplicated genes is the Slit-Robo Rho GTPase-activating protein 2 (*SRGAP2*) [14,18,21–25]. Multiple *SRGAP2* paralogs arose over the last ~3.4 million years, resulting in a conserved ancestral full-length *SRGAP2* and three truncated human-specific paralogs (*SRGAP2B*, *SRGAP2C*, and a likely nonfunctional *SRGAP2D* [23]), all located on human chromosome 1 (Figure 1A, top). The human ancestral *SRGAP2A* encodes a protein with F-BAR, RhoGAP, and SH3 domains, while *SRGAP2B* and *SRGAP2C* encode only F-BAR domains [26]. SRGAP2 forms homodimers with itself through the F-BAR domain; SRGAP2B and SRGAP2C dimerize with the F-BAR domain of SRGAP2A, leading to degradation of the resulting heterodimer via the proteasome pathway [21,24]. SRGAP proteins modulate cytoskeleton dynamics and promote membrane deformation when dimerized impacting vital cellular processes such as motility, polarity, and morphogenesis [26] (Figure 1A, bottom).

Mouse *Srgap2* has important functions in synapse maturation and connectivity via interactions with Homer, Gephyrin, and Rac1, the known regulators of both excitatory and inhibitory synapse maturation [18,24]. Mouse models expressing human *SRGAP2C* consistently phenocopy *Srgap2* knockdown and conditional knockout mice, showing conserved functional antagonism between the human and mouse proteins. These models exhibit increases in the rate of neuronal migration, neurite outgrowth, and density of dendritic spines, as well as neoteny in the spine maturation process [18,21,24]. Expressing *SRGAP2C* also increases long-range synaptic connectivity in mouse cortical pyramidal neurons and enhanced cortical processing abilities in the whisker-based texture-discrimination tests [22]. Together, these studies support the contribution of *SRGAP2C* to the emergence of unique neuronal features and cognitive capacities in humans.

Human-specific traits exist beyond the neocortex, including alterations in the development of musculoskeletal features and the eye [27]. The broad expression of *SRGAP2* paralogs in human cells and tissues [6] suggests it may have functions outside of neurons. However, the embryonic lethality of complete *Srgap2* loss-of-function in mouse models [28] allows limited assessment of its global functions. Here, we report that zebrafish *srgap2* "knockout" models result in viable offspring, allowing us to characterize *SRGAP2* developmental functions beyond the neocortex. We compared s*rgap2* knockouts with *SRGAP2C*-expressing "humanized" larvae in a range of morphological, gene expression, cellular, molecular, and behavioral assays. We observed concordant effects in *srgap2* knockout and *SRGAP2C*-humanized larvae across all assays, demonstrating that human-specific SRGAP2C antagonizes zebrafish Srgap2 functions and verifying previous known functions of *SRGAP2* as an axon/synapse regulator. We found zebrafish mutants exhibit increased susceptibility to seizures, strengthening previous findings in a human patient [29], present evidence that *SRGAP2* is a conserved core gene in microglia function across vertebrates that alters membrane dynamics and delays maturation, and propose a never-before-reported role of *SRGAP2* in the developing eye that impacts vision. Combined, our zebrafish models support previous studies in mice and expand on exciting new functions of *SRGAP2C*, opening new lines of inquiry related to microglia and the retina in the evolution of human-specific traits.

110 # Results

111 ## Genomic and transcriptional conservation of the zebrafish *srgap2* ortholog

112 The current zebrafish genome (GRCz11/danRer11) carries a single *srgap2* ortholog encoding F-BAR,
113 RhoGAP, and SH3 domains. Human full-length SRGAP2 and zebrafish Srgap2 proteins share 73.8%
114 amino acid identity, placing them phylogenetically closer to each other than to other members of the
115 SRGAP protein family (Figure 1A). The F-BAR domain of zebrafish Srgap2 shares 87.9% amino acid
116 identity with that of human SRGAP2. Computationally-predicted [30] probabilities of interaction between
117 SRGAP2C and zebrafish Srgap2 were comparable to those between SRGAP2C and mouse Srgap2 [18,21,24]
118 (Table S1). We experimentally confirmed heterodimer formation between zebrafish Srgap2 and human-
119 specific SRGAP2C by performing co-immunoprecipitation in HEK293T cells (Figure 1B).
120
121 Published whole-embryo RNA sequencing (RNA-seq)[31] showed that expression of *srgap2* continues to
122 increase after fertilization, plateaus after around 16 hours post fertilization (hpf), and persists thereafter;
123 we confirmed this expression pattern with quantitative RT-PCR (Figure 1C). Thus, the initiation of
124 *srgap2* expression coincides with critical neurogenesis periods, including the formation of post-mitotic
125 neurons in the neural plate after gastrulation [32] between 5.25 and 10 hpf [33]. Tissue-specific RNA-seq data
126 from embryos (24 hpf) and adults (12 months old) [34] showed high *srgap2* expression in the embryonic
127 head and adult brain with lower expression in viscera (e.g., heart, spleen, and kidney; Figure 1D). To
128 validate these results, we performed whole-mount *in situ* hybridization and observed *srgap2* expression
129 mainly in the developing central nervous system at 24 hpf and 3 days post fertilization (dpf) (Figure 1E).
130 Overall, *srgap2* expression is spatiotemporally regulated during a critical period of early
131 neurodevelopment in the zebrafish embryo and remains high in the adult brain [34]. These results suggest
132 that zebrafish can serve as a suitable model to test *SRGAP2* paralog functions during neural development.
133

134 ## *SRGAP2C* humanized larvae phenocopy *srgap2* knockout models

135 We evaluated *SRGAP2* function during development using two different zebrafish knockout models
136 (Figure 1F). First, we generated a stable *srgap2* knockout line carrying a 5-bp deletion in exon 4 using
137 CRISPR-Cas9 mutagenesis (*srgap2*$^{tup\Delta 5}$, Table S2). While stable mutant zebrafish lines are classically
138 used to test gene function [35,36], we also created mosaic embryos carrying a mixture of *srgap2* knockout
139 alleles by injecting ribonucleoproteins containing SpCas9 coupled with four different guide RNAs
140 (gRNAs) targeting early exons (termed "G_0 knockouts") [37–40]. Evaluation of control (wild type (WT) or
141 scrambled-injected) and mutant larvae revealed significantly decreased *srgap2* mRNA abundance at 5 dpf
142 in both knockout models (average relative reductions versus WT: Het= 23.8%, Hom= 59.7%, G_0
143 knockouts= 55.6%; Figure S1A). We observed no detectable off-target mutations in knockout larvae from
144 either approach at the most probable sites predicted using CIRCLE-Seq and CRISPRScan (Table S3),
145 suggesting that any observed phenotypes were due to the loss of Srgap2 function.

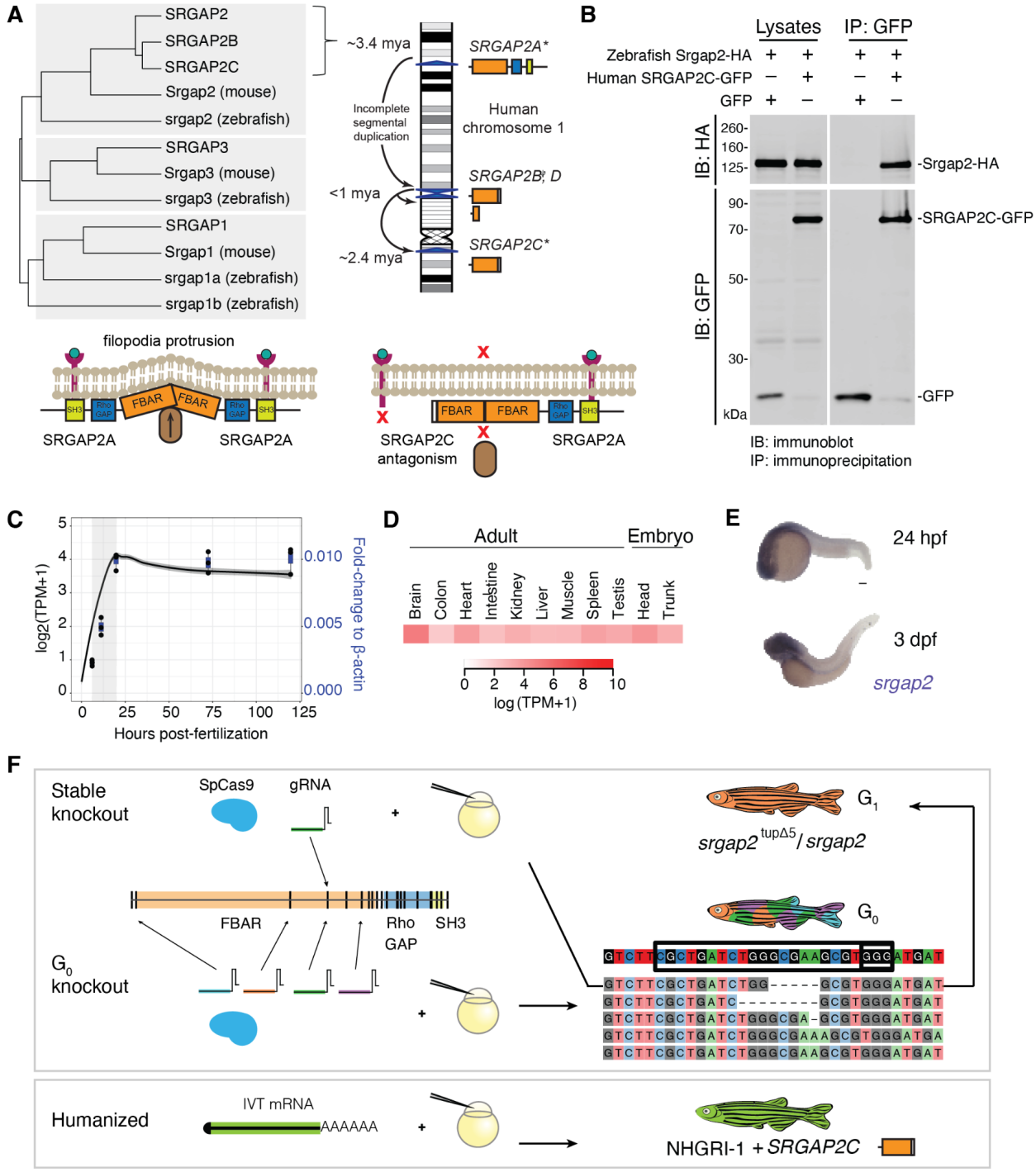

Figure 1. Functional analysis of *srgap2* in the developing zebrafish. (A) Top left, phylogenetic tree of human, mice, and zebrafish SRGAP proteins based on their full length amino acid sequence using the Unweighted Pair Group method with Arithmetic Mean method. Top right, schematic of inferred *SRGAP2* gene family evolutionary history across human chromosome 1 [25]. Bottom, cartoon summarizing the results of previous studies, showing that SRGAP2 functions after homodimerization in concert with F-actin (brown oval) to dictate cell membrane dynamics (bottom left) or heterodimerize with SRGAP2C producing no functional product (bottom right). **(B)** Co-immunoprecipitation of human-specific SRGAP2C and zebrafish Srgap2 in HEK293T cells showed interaction between these proteins. **(C)** Temporal expression of *srgap2* in the developing embryo according to publicly available RNA-seq data [31] (black line represents the best fit line with the standard error in dark gray) and normalized

quantitative RT-PCR data from whole-embryo RNA collected at 6, 10, 24, 72, and 120 hpf (blue boxes, each dot represents a biological replicate). The light-gray box represents a critical stage in zebrafish neurogenesis between 6 and 24 hpf [32]. (**D**) *srgap2* expression in embryonic (24 hpf) and adult (>12 months old) tissues from a published RNA-seq dataset [34]. (**E**) Spatial endogenous expression of *srgap2* at 24 hpf and 3 dpf via *in situ* hybridization shown in blue. Scale bar 100 µm. **(F)** Illustration of the approaches to creating knockout *srgap2* zebrafish. Top, a stable knockout line was generated by injecting SpCas9 coupled with one gRNA targeting exon 4. Middle, G_0 knockouts were generated by co-injecting SpCas9 coupled with four gRNAs targeting early exons. Bottom, humanized larvae were created by injecting *in vitro* transcribed *SRGAP2C* mRNA at the one-cell stage.

Homozygous (Hom) or heterozygous (Het) siblings produced from crossing *srgap2* knockout (Het) parents showed no difference in mortality at 5 dpf from WT siblings (survival curve test: χ^2= 2.96, df= 2, *p*-value= 0.228, n=148, WT= 19%, Het= 53%, Hom= 28%). G_0-knockouts also showed similar mortality to scrambled gRNA controls (χ^2= 0.3, df= 1, *p*-value= 0.6, n G_0-knockouts= 347, n controls= 260). However, we observed significant reductions in the length of the body axis (~4.4–7.6%) and distance between the eyes (~1.5–4.7%) of all *srgap2* knockout larvae (Het, Hom, and G_0) versus controls (Figure 2A). No significant effects on head-trunk angle, a feature typically used to estimate developmental timing in early zebrafish larvae [33], nor head area were observed, allowing us to rule out developmental delay (Figure 2A, S1B). Given the similarity of morphological features in both stable and mosaic knockout models, we primarily focused on phenotypes produced in G_0 knockout mutants moving forward.

Next, we generated a *SRGAP2C* humanized model by microinjecting *in vitro* transcribed mRNA into one-cell stage embryos (Figure 1F). This produced transient and ubiquitous presence of *SRGAP2C* transcripts in the developing zebrafish up to 72 hpf (Figure S1A), coinciding with peak endogenous *srgap2* expression (starting at 16 hpf; Figure 1C), with protein likely persisting for longer. *SRGAP2C*-humanized larvae developed normally with no increased mortality (survival curve test: χ^2= 0.8, df= 1, *p*-value= 0.4, *SRGAP2C*-injected= 422, eGFP-mRNA-injected controls= 308). They exhibited significant changes in overall body length and distance between the eyes (~5.7% reduction in body length and ~4.2% reduction in distance between the eyes Figure 2A), similar to the phenotypes observed in the knockout models. Thus, introducing human SRGAP2C antagonized endogenous zebrafish Srgap2 function in developing zebrafish larvae, similar to what has been observed in the mouse models [14,18,21,24].

Transcriptomes reveal developmental impacts upon perturbation of Srgap2 function

Given that knocking out *srgap2* and expressing human *SRGAP2C* generated similar developmental phenotypes (Figure 2A), we reasoned that a common set of molecular processes were perturbed under these two experimental conditions. To test this, we performed RNA-seq of dissected heads from G_0 knockouts and *SRGAP2C*-injected embryos/larvae across early developmental stages and performed differential expression analysis versus respective controls. From this, we observed high correlation of expression changes (Figures 2B and C, Note S1) and significant enrichment of shared differentially expressed genes (DEGs) between the knockout and humanized models (e.g., 467 shared genes at 5 dpf, Fisher's exact test odds ratio= 378.3, *p*-value < 2.2×10^{-16}, Table S4). We next assessed enriched gene ontology (GO) of shared DEGs between *srgap2* G_0 knockout and *SRGAP2C* humanized larvae (which we collectively term "*SRGAP2* mutants") to understand molecular changes in these models.

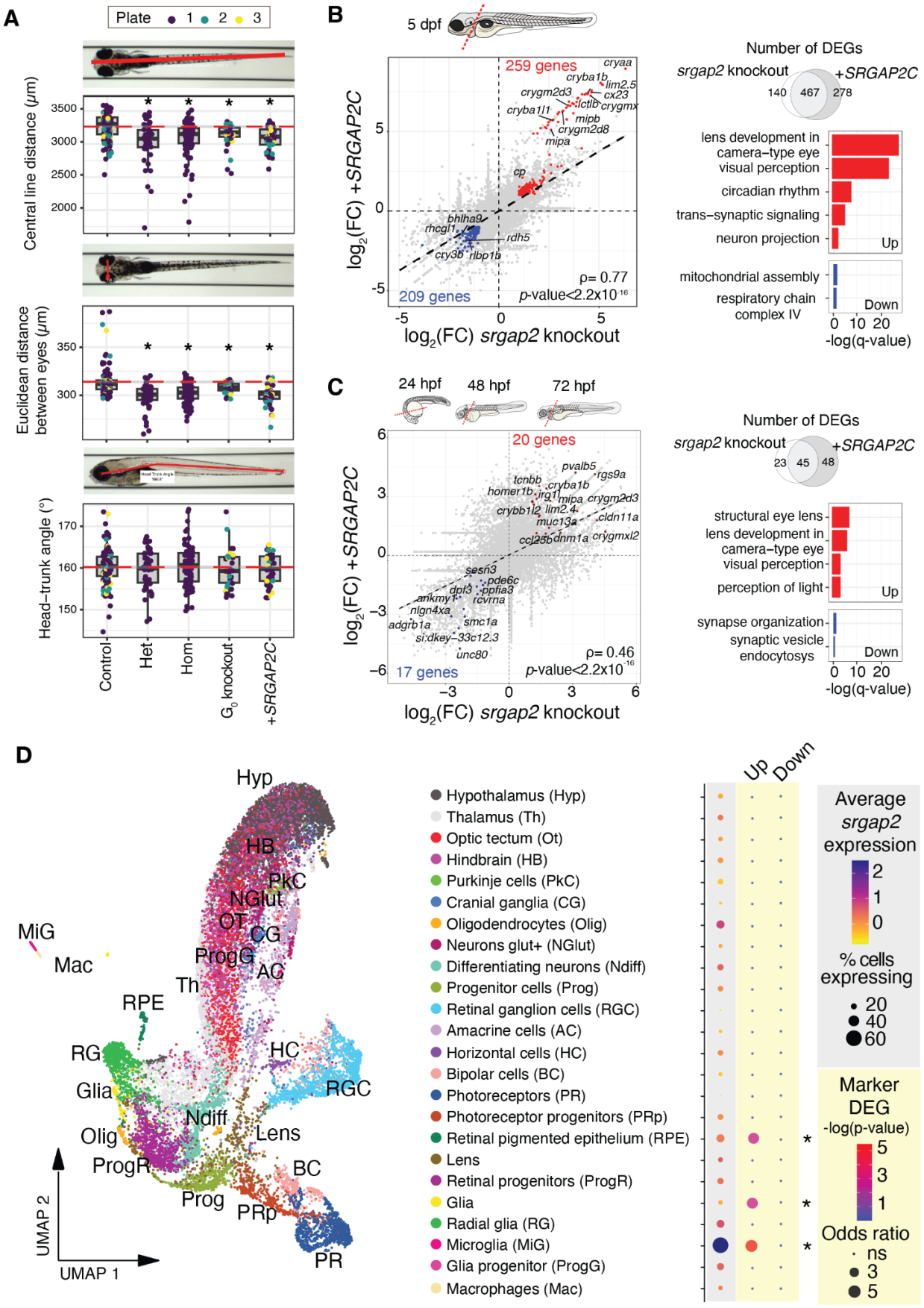
A
Plate 1 2 3
Central line distance (μm)
Euclidean distance between eyes (μm)
Head–trunk angle (°)
Control
Het
Hom
G0 knockout
+SRGAP2C
B
5 dpf
259 genes
209 genes
ρ= 0.77
p-value<2.2x10-16
log2(FC) +SRGAP2C
log2(FC) srgap2 knockout
Number of DEGs
srgap2 knockout
+SRGAP2C
140 467 278
lens development in camera–type eye
visual perception
circadian rhythm
trans–synaptic signaling
neuron projection
Up
mitochondrial assembly
respiratory chain complex IV
Down
-log(q-value)
C
24 hpf
48 hpf
72 hpf
20 genes
17 genes
ρ= 0.46
p-value<2.2x10-16
log2(FC) +SRGAP2C
log2(FC) srgap2 knockout
Number of DEGs
srgap2 knockout
+SRGAP2C
23 45 48
structural eye lens
lens development in camera–type eye
visual perception
perception of light
Up
synapse organization
synaptic vesicle endocytosys
Down
-log(q-value)
D
Hyp
HB
PkC
NGlut
OT
CG
MiG
Mac
ProgG
AG
Th
RPE
RG
HC
Glia
RGC
Ndiff
Olig
Lens
ProgR
BC
Prog
PRp
PR
UMAP 2
UMAP 1
Hypothalamus (Hyp)
Thalamus (Th)
Optic tectum (Ot)
Hindbrain (HB)
Purkinje cells (PkC)
Cranial ganglia (CG)
Oligodendrocytes (Olig)
Neurons glut+ (NGlut)
Differentiating neurons (Ndiff)
Progenitor cells (Prog)
Retinal ganglion cells (RGC)
Amacrine cells (AC)
Horizontal cells (HC)
Bipolar cells (BC)
Photoreceptors (PR)
Photoreceptor progenitors (PRp)
Retinal pigmented epithelium (RPE)
Lens
Retinal progenitors (ProgR)
Glia
Radial glia (RG)
Microglia (MiG)
Glia progenitor (ProgG)
Macrophages (Mac)
Up
Down
Average srgap2 expression
% cells expressing
Marker DEG -log(p-value)
Odds ratio
ns

198

Figure 2. Developmental and cellular phenotypes of diverse zebrafish models of *SRGAP2*. (**A**) Measurements of central line distance (ANOVA: $F_{(4, 321)}$= 12.84, genotype effects *p*-value= $1.04x10^{-9}$, FDR-adjusted *p*-values Het= $4.40x10^{-7}$, Hom= $6.29x10^{-7}$, Pooled= 0.015, *SRGAP2C*= $1.36x10^{-4}$), Euclidean distance between the eyes (ANOVA: $F_{(4,321)}$= 23.49, genotype effects *p*-value= $4.72x10^{-17}$, Dunnett's test FDR-adjusted *p*-values: Het= $6.77x10^{-11}$, Hom= $4.69x10^{-10}$, Pooled= 0.05, *SRGAP2C*= $2.19x10^{-9}$), and head angle (ANOVA: $F_{(4,315)}$= 0.49, genotype effects *p*-value= 0.746) in 5 dpf larvae from stable *srgap2* knockout (Het n= 43, Hom n= 86), G_0 knockouts (n= 34), *SRGAP2C*-injected (n= 44), and control larvae (n= 124). Dots represent an imaged larva with the color indicating the imaging plate (a co-variable included in the statistical analyses). The red dotted line corresponds to the mean value for the control group. Representative images of each measurement are included on the top of each plot. (**B**) Correlation of the fold change (FC) between *srgap2* G_0-knockouts and *SRGAP2C*-injected larvae at 5 dpf, with common DEGs highlighted (red= upregulated (FC > 2), blue= downregulated (FC < -2)). Top representative GO terms enriched in common DEGs between *srgap2* G_0-knockouts and *SRGAP2C*-injected larvae (complete results in Table S5). Color of the bar represents the direction of the genes (red= commonly upregulated, blue= commonly downregulated). (**C**) Correlation of the FC between *srgap2* G_0-knockouts and *SRGAP2C*-injected larvae across development using data from 24, 48, and 72 hpf larvae, with common DEGs highlighted, complete results can be found in Tables S7, S8. (**D**) Clustering of the 28,687 profiled cells colored as 24 cell types based on the expression of gene markers. Expression of *srgap2* across cell types (left side, shaded in gray), with the size of the circle representing the percentage of cells in that cluster expressing *srgap2* and the color of the circle representing the average scaled expression in the cluster. Enrichment test for the overlap between marker genes for each cell type and the differentially expressed genes at 3 dpf from bulk RNA-seq data (right side), with the size of the circle representing the odds ratio for the enrichment and the color of the circle the -log(BH-adjusted *p*-value) of the Fisher's exact test. Asterisks indicate an FDR-adjusted *p*-value < 0.05.

We found that shared upregulated genes across all developmental time points were related to lens and visual system development in the *SRGAP2* mutant models (Tables S4–S8). Upregulated genes unique in older mutant larvae (5 dpf) were related to neurodevelopment (mainly neuronal projections and synapse organization) and circadian rhythm, and downregulated genes involved mitochondrial cytochrome c oxidase assembly (Figures 2A). Mitochondrial dysfunction is associated with reduced height [41], consistent with the reduced body axis observed in *SRGAP2* mutant larvae. Young mutant embryos (1, 2, 3 dpf) exhibited downregulation of genes related to synapse organization relative to the controls, suggesting delayed synaptic maturation. In particular, *ppfia3*, a regulator of presynapse assembly [42], was found significantly upregulated in 5 dpf mutant larvae while downregulated in mutant embryos (≤ 3 dpf). These results align with the neoteny of synaptogenesis observed in *Srgap2* knockdown or *SRGAP2C*-expressing mouse embryos [18]. In summary, identifying the common pathways affected in the *srgap2* knockout and *SRGAP2C*-humanized zebrafish models provide evidence of the critical role that the genes play in the development of the visual system and neurodevelopment.

To narrow in on the cell types driving expression changes, we performed transcriptomic profiling (SPLiT-seq [43]) of 28,687 single cells isolated from 3 dpf zebrafish larval brains of *SRGAP2* mutants and controls (Table S9). Using expression patterns of marker genes [44,45], we classified 24 cell types and found broad endogenous *srgap2* expression across neuron-containing clusters, with highest expression in microglia (Figure 2D, Tables S10 and S11). We observed a significant enrichment of upregulated DEGs we associated with *SRGAP2* mutants through bulk RNA-seq analysis (Figure 2C) in markers for retinal pigmented epithelium (RPE), glia, and microglia cells (Table S12).

Synaptic alterations in *SRGAP2* zebrafish models

Based on the broad neural expression of *srgap2*, we next performed differential pseudo-bulk differential expression analysis using 11,450 neuronal cells. Shared upregulated genes between *SRGAP2* mutant models (n=14) related to neuron projection guidance (Figure 3A), including *ephb2*, which is implicated in promoting/directing axon guidance across the brain midline [46,47]. Shared downregulated genes (n=21) were enriched for synaptic signaling functions, concordant with bulk RNA-seq results (Figure 3A, Tables S13 and S14). With respect to neuronal subtypes, markers for forebrain (comprising the telencephalon and orthologous to the mammalian neocortex [48,49]), midbrain (composed of optic tectum, the visual processing center in the zebrafish brain [50]), and differentiating neurons were enriched in upregulated genes; while hindbrain and the broad neuron category were enriched for downregulated genes (Figure 3A, Table S15, BH-adjusted Fisher's exact tests *p*-values < 0.05).

Given findings of altered synaptic signaling/organization in mutant zebrafish (Figure 2B) and the role of *SRGAP2* paralogs in regulating synapses in mice [18] , we narrowed in on excitatory (Exc; *slc17a6b*/*vglut2*) and inhibitory (Inh; *gad1b*) neuronal subtypes in our scRNA-seq data [44,45]. Comparing relative abundances across models showed that both *srgap2* knockouts and *SRGAP2C*-injected larvae exhibited a ~20% increase in the Exc:Inh ratio (Figure 3B). Quantifying co-labeled GABAergic (Tg[*dlx6a*:GFP] [51]) and glutamatergic (Tg[*vglut2a:*DsRed] [52]) neurons validated these results, with a ~29% increase in the Exc:Inh ratio relative to uninjected wild-type and control-injected larvae (Figure 3C). The ratio measured in our controls matched that from previous studies using the same transgenic lines of the same age [53] (wild-type controls Exc:Inh ratio= 0.98±0.04).

A skew towards excitatory versus inhibitory neuronal balance is associated with seizures, as has been reported in several zebrafish epilepsy models [54]. We therefore assessed chemically-induced seizure-like behaviors in control and *SRGAP2* mutant models [55]. We counted high-speed movement events (HSE, >28 mm/s) in 4 dpf larvae exposed to either a low concentration of pentylenetetrazol (PTZ, 2.5 mM) or to E3 media (control). While HSE were rare in non-PTZ-treated larvae with no difference in frequency between genotypic groups (average HSE/min= 0.006±0.02; Figure 3D), the addition of PTZ significantly increased the frequency of HSE on average by 0.31±0.08 min^{-1} in *srgap2* knockouts and *SRGAP2C*-humanized larvae compared to controls. Next, we detected spontaneous electrographic seizures by recording local field potentials (LFP) [55]. *SRGAP2C* larvae demonstrated ictal-like Type II electrical events, classifying them as epileptic (n= 21, LFP score= 1.45, Figure 3E), while control (n= 22) and *srgap2* G_0-knockouts (n= 30) did not exhibit any events. Strikingly, *SRGAP2C* larvae showed LFP scores in the range observed in zebrafish models of well-established epilepsy-associated genes (e.g., *SCN1A*, *STXBP1*) [55]. Overall, our results point to a role for SRGAP2 and its human-specific paralog *SRGAP2C* in maintaining neuronal E:I balance and potentially contributing to seizure susceptibility.

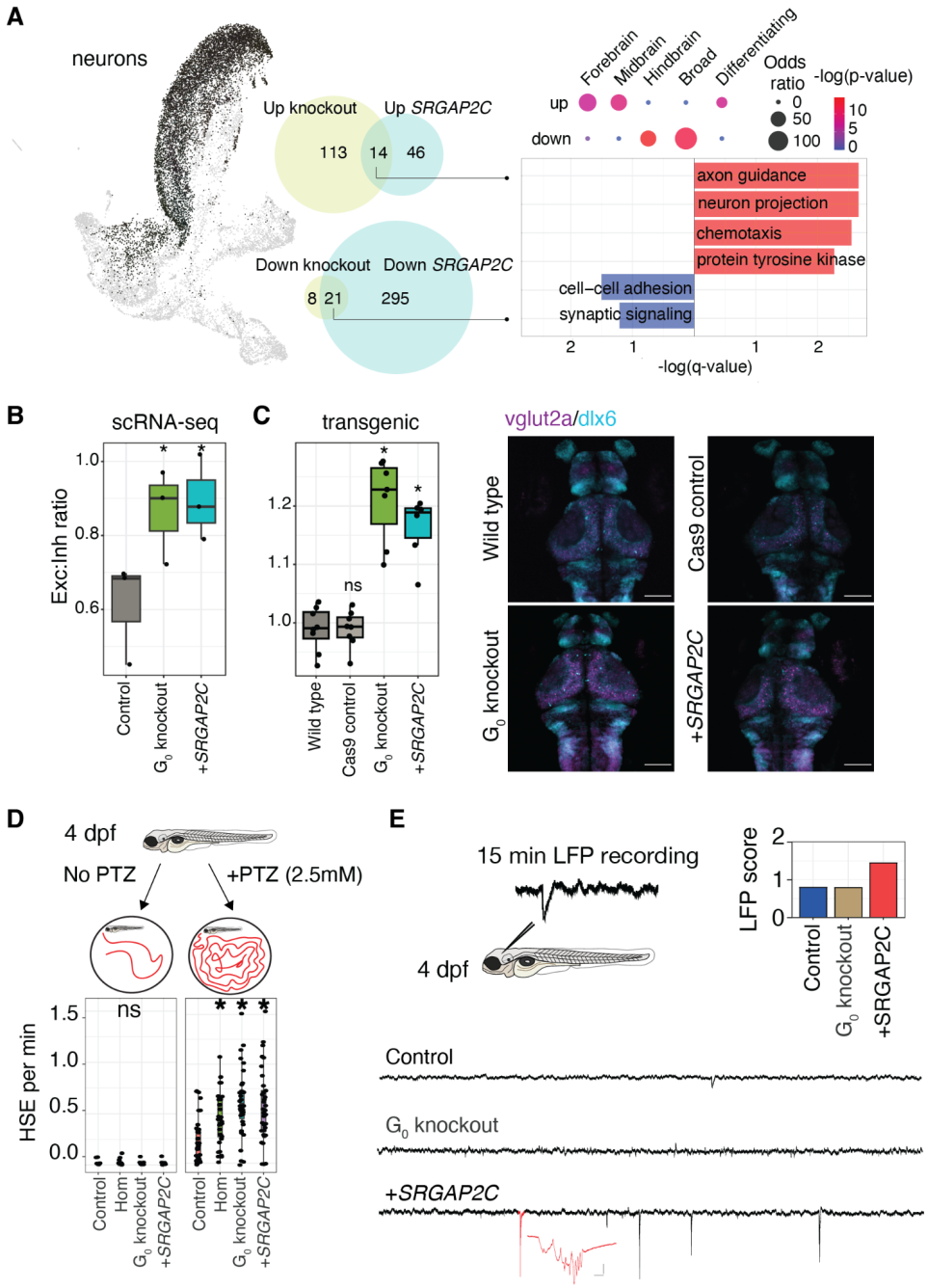

Figure 3. Neuronal alterations in *SRGAP2* mutants. (**A**) Neuronal clusters (hypothalamus, thalamus, optic tectum, hindbrain, Purkinje cells, and neurons rich in glutamate receptors) selected to perform a differential gene expression test was performed to DEGs in the *SRGAP2* mutants compared to the control group. Bar plot represents the top GO terms overrepresented in the 14 commonly upregulated genes (complete results in Table S14). (**B**) Ratio of cells classified as excitatory (*vglut2*$^+$) to inhibitory (*gad1b*$^+$) between the *srgap2* G_0-knockouts, *SRGAP2C*-injected, and controls (*srgap2* G_0 knockouts: 0.78±0.15, *p*-value= 0.031; *SRGAP2C*-injected: 0.82±0.09, *p*-value= 0.017, controls= 0.57±0.13; t-tests versus controls). (**C**) Ratio of excitatory (*vglut2*:DsRed+) to inhibitory (*dlx6*:GFP) cell area quantified from images of 3 dpf *srgap2* G_0-knockout, *SRGAP2C*-injected, SpCas9 control injected, and uninjected wild type larvae (G_0 knockout: Exc:Inh ratio=1.21±0.07, *p*-value=3.0x10^{-4}, *SRGAP2C*: Exc:Inh ratio= 1.16±0.05, *p*-value= 7.0x10^{-4}, SpCas9-injected controls Exc:Inh ratio= 0.98±0.03, p-value= 0.959; Mann-Whitney U-tests *p*-values vs wild-type controls). Images include representative samples per group, scale bars 100 µm. (**D**) High-speed events (HSE, >28 mm/s) identified in 15 min recordings of 4 dpf larvae (*srgap2* knockouts

293 (stable Hom_{parent} and G_0), *SRGAP2C*-injected, and SpCas9-injected controls, n= 36 larvae per group) with and
294 without PTZ. Frequency of HSE per min were compared to controls (0 mM PTZ: ANOVA *p*-value for genotypic
295 effect= 0.415, average HSE/min= 0.006±0.02, no significant differences between groups; 2.5 mM PTZ: ANOVA
296 genotype effect *p*-value= $1.1x10^{-6}$, Hom_{parent}= 0.010, G_0-knockouts= $2.2x10^{-6}$, *SRGAP2C*-injected= $3.90x10^{-5}$). **(E)**
297 Local field potential (LFP) recordings in the optic tectum of 4 dpf larvae (G_0-knockouts, *SRGAP2C*-injected, and
298 SpCas9-injected controls, n=21-30 per group) were obtained and scored by two independent researchers.
299 Representative traces per group are shown. Asterisks in graphs represent a *p*-value below 0.05 for the comparison
300 against the control group. ns= not significant.
301

302 ## ***SRGAP2* is a conserved microglial gene that inhibits cell ramifications**

303 While *SRGAP2* functions are well-characterized in neurons, we observed the highest expression of *srgap2*
304 in microglia (Figure 3D). This observation is concordant with a previous study implicating *SRGAP2* as a
305 "core" microglia gene with high conservation across human, macaque, marmoset, sheep, rat, mouse,
306 hamster, and zebrafish [56]. When comparing the transcriptomes of microglia cells from *srgap2* knockout
307 and *SRGAP2C*-expressing zebrafish models versus their respective controls, we found that shared
308 upregulated genes (n=38) were implicated in cell migration and shared downregulated genes (n=65) were
309 related to actin-mediated filopodia processes (Figure 4A, Tables S16 & S17). These results align with the
310 ability of SRGAP2 to induce cell projections in concert with F-actin in a variety of systems [57,58]. Since
311 microglia also develop complex cell ramifications, we hypothesized that their cell-membrane dynamics
312 were also modulated by Srgap2 activity.
313
314 To test this, we characterized microglia in *srgap2* G_0 knockouts and humanized *SRGAP2C* models. While
315 there was no difference in microglia abundance between genotypes [59] (Figure S2), we observed
316 significantly reduced ramifications (quantified as increased sphericity) for both knockout and humanized
317 larvae compared to controls at both 3 and 7 dpf using a transgenic line labeling macrophages
318 (Tg[*mpeg1.1*:GFP], Figure 4B) [60]. By these developmental time points, macrophages are generally
319 accepted to be microglia (or their precursors) when localized in the brain/retina of zebrafish [61]. The
320 microglia in control larvae continued to acquire more ramified morphologies from 3 to 7 dpf as they
321 matured (t-test of 3 vs 7 dpf: t= 2.97, *p*-value= 0.0055, Figure 4B), concordant with previous reports [62].
322 Microglia in both *srgap2* mutant models retained similar sphericity at both timepoints (t-tests per mutant
323 genotype *p*-values > 0.05), suggesting arrested maturation. However, we cannot rule out increased
324 microglia activation, which also involves morphological changes from a ramified "resting" state to more
325 ameboid-like active shapes [63,64]. This interpretation is supported, in part, by the upregulation of known
326 microglial activation markers (*hsp90aa1.1* and *zfp36l2*) observed in our *SRGAP2* mutants at 5 dpf [65] from
327 bulk RNA-seq results (Figure 2B).
328
329 To ask if SRGAP2/C might contribute to human-specific microglia membrane dynamics, we re-analyzed
330 published single-cell transcriptomes of 610,596 prefrontal cortex cells from human, chimpanzee,
331 macaque, and marmoset [66]. In line with its conserved "core" characterization [56], *SRGAP2* exhibited
332 highest expression in the microglia clusters in all primates (Figure 4C), including human- and Hominidae-
333 specific microglia subclusters (Figure 4D, Note S2, Table S18). *SRGAP2C* expression was also high in all
334 human microglia subtypes, albeit slightly lower compared to *SRGAP2*. Taking a pseudo-bulk approach
335 analogous to the zebrafish analysis (Figure 3A), we compared differential expression of human
336 (+*SRGAP2C*) versus chimpanzee, macaque, or marmoset (-*SRGAP2C* "controls") microglia. Human
337 DEGs were consistent with reduced microglia ramifications, including downregulation of genes

338 associated with cell projection and the plasma membrane (Table S19). We also observed the upregulation
339 of genes implicated in extracellular matrix and inflammatory response, both features of migrating
340 microglia in an ameboid state. Comparing DEGs between human/primate and zebrafish *SRGAP2* mutants
341 revealed significant overlap (10 genes, Fisher's test odds ratio= 2.77, *p*-value= 0.0046). Thus, the
342 alterations of microglial cell shape observed in our zebrafish *SRGAP2C* "humanized" models were
343 recapitulated in human-specific biological processes that occur in microglial cells.
344

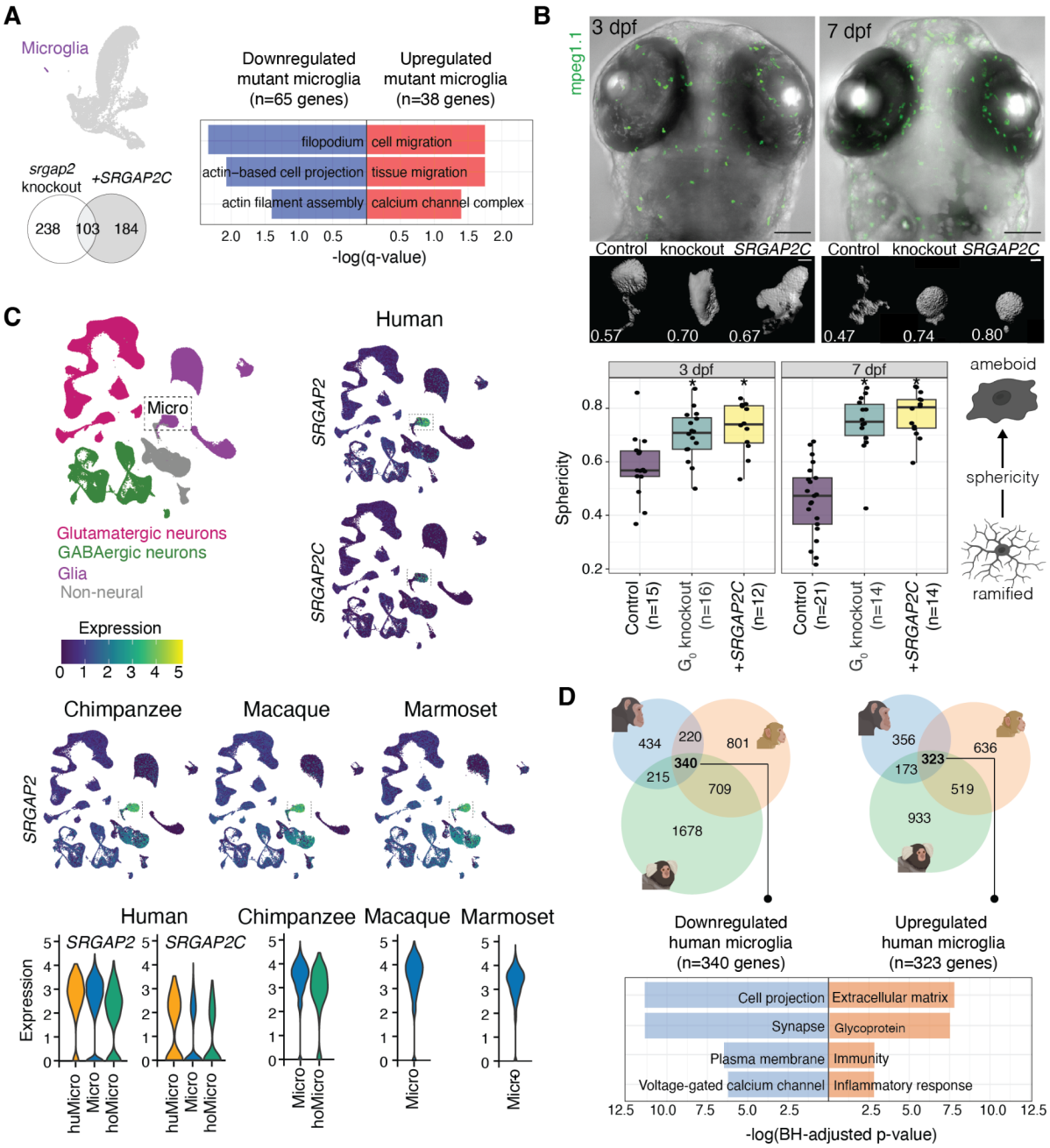

345

346 **Figure 4. Cross-species conservation of *SRGAP2* as a microglial gene.** (**A**) Top GO terms with significant
347 overrepresentation in genes upregulated (red) or downregulated (blue) in microglial cells from *SRGAP2* mutants
348 from Figure 2D. (**B**) Sphericity values for individual microglial cells (mpeg1.1^{+}) at 3 and 7 dpf in *srgap2* knockouts,
349 *SRGAP2C*-injected, and scrambled gRNA-injected controls. Each dot represents a single microglial cell (average of

350 4-5 cells per larvae from 3-4 larvae per genotype per timepoint were obtained). Representative images for the
351 median sphericity value of larvae at 3 and 7 dpf for each genotype are included below the graph (scale bars: top
352 images= 100µm, bottom images= 5 µm) . Asterisks denote a Tukey *post*-hoc p-value < 0.05. 3dpf: *srgap2* G_0
353 knockouts: 0.70±0.09, *p*-value= 0.0085; *SRGAP2C*-injected: 0.73±0.09, *p*-value= 0.0021, controls: 0.58±0.12; 7dpf:
354 *srgap2* G_0 knockouts: 0.74±0.11, *p*-value < $2.2x10^{-16}$; *SRGAP2C*-injected: 0.78±0.08, *p*-value < $2.2x10^{-16}$, controls:
355 0.46±0.13. (**C**) Evaluation of 610,596 prefrontal cortex cells from human, chimpanzee, macaque, and marmoset
356 (human: 171,997, chimpanzee: 158,099, macaque: 131,032, marmoset: 149,468) showing the levels of *SRGAP2* and
357 *SRGAP2C* expression across species, highlighting the microglial cluster with a dotted square. Micro: microglia.
358 Expression of *SRGAP2* and *SRGAP2C* in microglial subtypes across species with subtypes ordered from highest
359 expression left to right. huMicro: human-specific microglia, hoMicro: Hominidae-specific microglia. **(D)** Microglial
360 cells from human, chimpanzee, macaque, and marmoset (human: 8,819 cells, chimpanzee: 6,000 cells, macaque:
361 9,000 cells, marmoset: 7,099 cells) from the prefrontal cortex and middle temporal gyrus were used to identify
362 common DEGs between human and non-human primates, finding 340 common upregulated and 323 common
363 downregulated genes. Top GO terms with significant overrepresentation in common DEGs are included.
364

365 **Visual system alterations in *SRGAP2* zebrafish models**

366 The most striking molecular change in *SRGAP2* mutant zebrafish was the upregulation of genes related to
367 lens development and visual perception (Figure 2B & C). Performing RNA *in situ* hybridization (ISH) of
368 the developing zebrafish eye, we found predominant endogenous *srgap2* expression in the optic nerve
369 (ON), RPE, and along the retinal ganglion cell layer (GCL) at 3 dpf (Figure 5A). While scRNA-seq data
370 showed strong expression of *srgap2* and enrichment of differential marker genes in RPE cells, we found
371 little to no *srgap2* expression in retinal ganglion cells (RGCs) comprising the GCL (Figure 2D). Instead,
372 *srgap2* ISH likely marks microglia that have migrated into the retina, with strongest expression evident at
373 the interface between the lens and the neural retina.
374
375 To understand biological impacts within the retina, we identified DEGs across RGCs and RPE cells in
376 *SRGAP2* mutants versus controls. RGCs were enriched for shared upregulated genes related to stem-cell
377 differentiation, neuron-projection extension, and amoeboid-type cell migration (Figure 5B, Tables S20 &
378 S21). Shared upregulated genes in RPE were also associated with cell-cell adhesion as well as negative
379 regulation of the smoothened pathway, which mediates response to Hedgehog signaling [67]. Shared
380 downregulation of genes important in extracellular structures (e.g., matrix metalloproteinases, laminin,
381 and collagen gene families) was observed in both RGCs and the RPE. Connecting our findings to the
382 developing human retina (organoids [68,69] and post mortem [70,71]), transcriptomic data from human
383 (+*SRGAP2C*) versus rhesus macaque (-*SRGAP2C* "controls") also show upregulation of similar pathways
384 related to axon development and neuron projections. Again, we observed a significant overlap in common
385 DEGs between cells from human retina and *SRGAP2* zebrafish mutant RGC/RPE (69 genes, Fisher's test
386 odds ratio= 6.23, *p*-value< $2.2x10^{-16}$; Tables S22-S25 and Note S3). Importantly, the eyes of *srgap2*
387 knockout and *SRGAP2C*-humanized zebrafish developed normally with the formation of all major cell
388 types by 5 dpf, indicating that these changes in gene expression did not affect gross aspects of eye
389 development (Figure S3). Together, these results point to unexplored human-specific eye development
390 features facilitated by SRGAP2C—related to membrane dynamics impacting axonogenesis—altering
391 retinal connectivity that is fundamental for visual information processing [72].
392

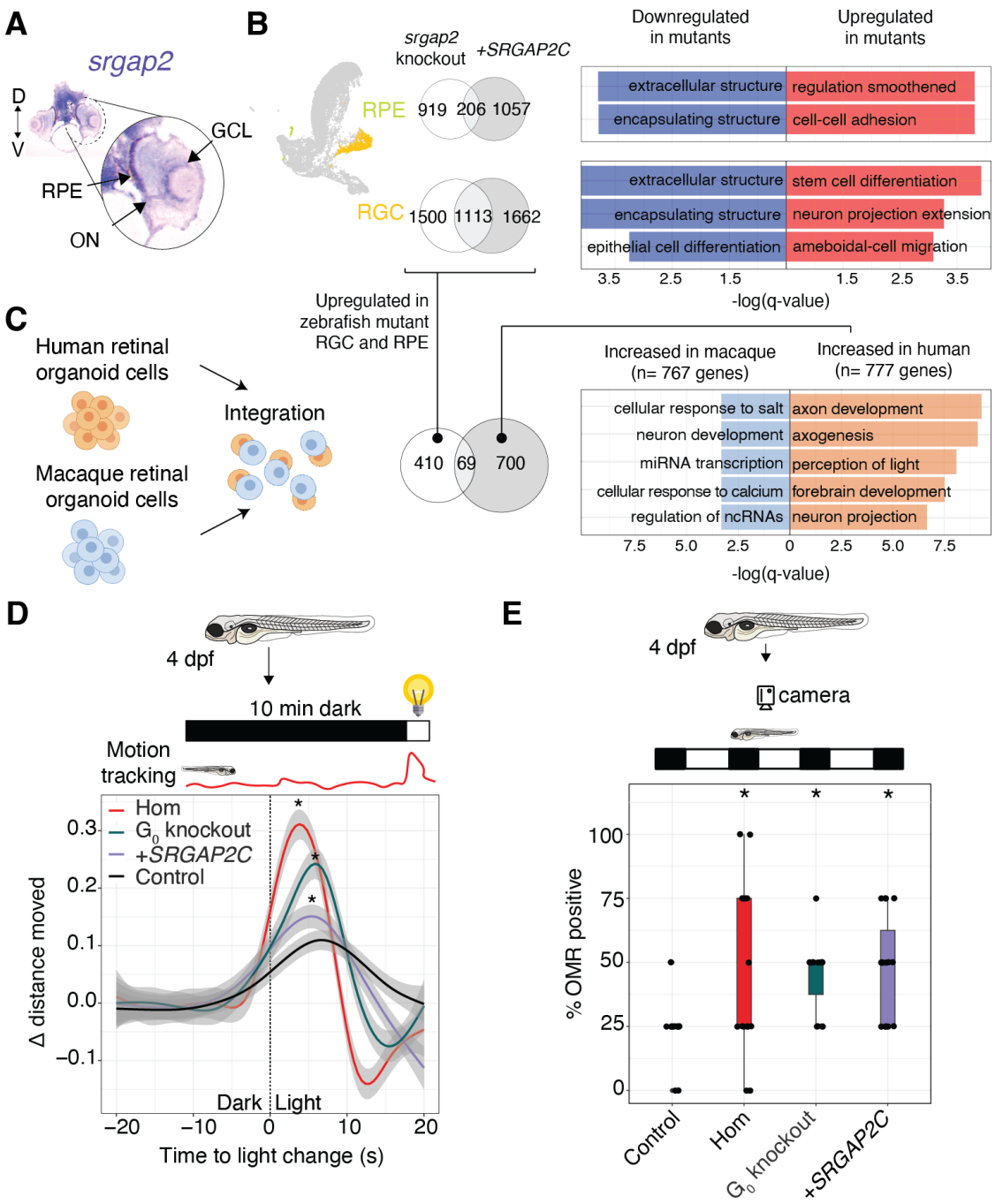

Figure 5. *SRGAP2* impacts the retina. **(A)** Section of a 3 dpf NHGRI-1 larva staining *srgap2* expression via *in situ* hybridization, labeling predominantly the optic nerve (ON), retinal pigmented epithelium (RPE), and the ganglion cell layer (GCL). D: dorsal, V: ventral. **(B)** Retinal ganglion cells (RGCs) were selected and a differential gene expression performed between *SRGAP2*-mutants (*srgap2* knockouts and *SRGAP2C*-injected) versus controls, identifying 60 upregulated genes and 84 downregulated genes, with their top overrepresented GO terms included in bar plots. **(C)** Human and macaque cells from retinal organoids (43,857 human and 19,894 macaque) were integrated to identify genes with increased expression in either species, with their top overrepresented GO terms included in bar plots (complete results in Tables S22 and S23). **(D)** Motion response to changes in light were assessed in 4 dpf *srgap2* knockouts (Hom_{parent} and G_0-knockouts), *SRGAP2C*-injected, and SpCas9-scrambled gRNA-coupled control larvae using a 10 min acclimation period followed by an abrupt light change. Plot includes trend lines for change in distance moved observed in each evaluated group (n= 24 per group, standard error for each

405 line included as a shaded gray), which were different between all groups compared to controls (Kolmogorov-
406 Smirnov tests *p*-values: Hom_{parent}= 9.16x10^{-11}, G_0-knockouts= 5.93x10^{-8}, *SRGAP2C*-injected= 1.11x10^{-12}). (**E)**
407 Optomotor responses were evaluated in 4 dpf larvae using an optimized protocol[73] that quantifies the percentage of
408 larvae relative to moving stripes. Boxplot includes the percentage of OMR-positive larvae (aligned to the visual
409 stimulus) in *srgap2* knockouts (Hom_{parent} and G_0-knockouts) and *SRGAP2C*-injected, which was higher compared to
410 controls (Dunn's Benjamini-Hochberg adjusted *p*-values: Hom_{parent}= 0.0113, G_0-knockouts= 0.0040, *SRGAP2C*-
411 injected= 0.0040). Asterisks denote a *p*-value below 0.05.
412
413
414 To test if the observed differences in gene expression patterns are associated with altered vision, we
415 leveraged natural zebrafish larval behavior that react to abrupt changes in light intensity with increased
416 swimming activity [74,75]. Using motion tracking, we observed a significant increase in response (reaction
417 time and movement) to light stimulus in *srgap2* mutants (knockouts and *SRGAP2C*-injected) compared to
418 controls (Figure 5D) at 4 dpf, showing increased sensitivity to light changes. Considering our models
419 exhibited increased susceptibility to seizures, which could evoke similar responses, we also characterized
420 more refined visual cues. The optomotor response (OMR) measures the instinctive behavior of free-
421 swimming zebrafish larvae wherein they align their body axis in the same direction as contrasting visual
422 stimuli, such as moving stripes. This helps freshwater fish swim upstream [73,76,77]. We found that a larger
423 percentage of 4 dpf *srgap2* knockouts (Hom_{parent} and G_0) and *SRGAP2C*-humanized mutants showed
424 OMR-positive positioning compared to the control group (n per group= 15, Figure 5E). Together, these
425 results suggest that reduction in Srgap2 activity—either through genetic knockouts or expression of
426 human *SRGAP2C*—impacts the function of retinal microglia and possibly contributes to altered neuronal
427 connectivity in the developing eye, leading to more sensitive neuronal responses to visual cues.
428

429 # Discussion

430 *SRGAP2* is a well-studied human-specific duplicated gene with a wealth of gain- and loss-of-function
431 studies in diverse cell culture and mouse models. Its documented functions include regulating neuronal
432 migration, synaptogenesis, and long-range connectivity in the central nervous system [14,18,22,24]. However,
433 because of the embryonic lethality of the *Srgap2* knockout in mouse models, any roles beyond the
434 neocortex are still largely unexplored. Here, we present new functional analyses of *SRGAP2* in zebrafish,
435 where viable knockout mutants allow detailed screening of developmental phenotypes at an organismal
436 level. We observed an overall concordance in developmental phenotypes between *srgap2* knockouts and
437 *SRGAP2C*-injected zebrafish larvae, similar to previous mouse studies where temporal expression of
438 truncated *SRGAP2C* mirrored *Srgap2*-knockdown/knockout alleles [14,18,24]. For example, both *SRGAP2*
439 knockout and humanized models consistently exhibited shorter body length, a phenotype not reported
440 previously. This could be driven by altered mitochondrial functions as suggested by bulk RNA-seq
441 analysis (Figure 2B), or by perturbation to migration-dependent processes such as muscle guidance and
442 body patterning that are influenced by the Slit-Robo pathway [78,79]. No heterozygous loss-of-function
443 variants have been discovered in ancestral *SRGAP2* across hundreds of thousands of healthy humans to
444 date [80], indicating strong selective constraint (gnomAD pLI=0.87); moving forward, it will be interesting
445 to compare mutant phenotypes with those of human patients carrying gene-impacting mutations.
446
447 Bulk transcriptomic analyses of mutant zebrafish—ranging from 24 hpf embryos to 5 dpf larvae—
448 revealed alterations to known molecular functions, suggesting increased axonogenesis in *SRGAP2*
449 mutants consistent with the gene's well-characterized role in axonal guidance via the Slit-Robo pathway

450 [14]. Downregulation of genes related to synaptogenesis in early developmental embryos (24 hpf–3 dpf,
451 Figure 2C) is concordant with neoteny of synaptogenesis in *SRGAP2* mouse models reminiscent of
452 human brain development [18,24]. The single-cell transcriptomes allowed us to further narrow in on altered
453 neuronal functions (Figure 2D). For example, mutants exhibited skewed Exc:Inh balance of neurons that
454 manifested as increased susceptibility to chemically-induced seizures (Figure 3C). *SRGAP2C*-expressing
455 larvae also presented spontaneous, unprovoked, electrographic seizures not observed in our G_0 knockout
456 mutant. Differences in phenotypic severity between the knockout and humanized models might be
457 explained by genetic compensation due to nonsense-mediated decay in the knockout mutant [81].
458 Transcriptome data of *SRGAP2* mutant neurons provided additional clues to possible mechanisms
459 underlying the observed phenotypes; for example, we observed significantly reduced expression of the
460 *GRIN2A* ortholog (*grin2ab*, Table S13), encoding glutamate [NMDA] receptor subunit epsilon-1, with
461 loss-of-function variants implicated in epileptic aphasia in humans [82]. These results are largely consistent
462 with a clinical report of early infantile epileptic encephalopathy in a human child carrying a reciprocal
463 translocation disrupting *SRGAP2* [29], providing evidence that mutations of this gene may contribute to
464 epilepsy. We note that the embryonic lethality of *Srgap2* knockout mice has impeded similar evaluations
465 in mammalian models to date.
466
467 Hallmark studies have shown that *Srgap2* loss-of-function or *SRGAP2C* expression leads to reduced
468 filopodia in COS7 cells and fewer branching processes in mouse cortical neurons [14] altering neuronal
469 migration *in vivo* [21]. Similarly, we found that mutant zebrafish microglia exhibit reduced ramifications
470 versus controls, also evident in transcriptomes (reduced expression of filopodia and actin-based cell
471 projections-related genes and increased expression of cell migration genes). The mutant microglia also
472 maintained an ameboid-like spherical shape through development time (3 to 7 dpf; Figure 4B) instead of
473 the expected increased ramifications observed in a typically-developing zebrafish larva [62]. This ameboid-
474 like shape is indicative of either "active" or immature microglia. While we cannot rule out that mutant
475 microglia were more activated, we propose that microglia exhibited developmental delay like that
476 observed in synaptic spine maturation in mice [21]. Indeed, a recent preprint [83] showed similar microglia
477 neoteny in *SRGAP2C* mouse and human cell models. Interestingly, human adult microglia also express
478 *SRGAP2* paralogs and exhibit similar transcriptome differences with nonhuman primates as *SRGAP2C*-
479 humanized zebrafish microglia do with controls. Most overlapping DEGs function in actin-cytoskeleton
480 dynamics (down) and cell-cell interactions (up). This provides molecular evidence of altered membrane
481 dynamics of human microglia compared with other primates, consistent with the reduced ramifications
482 observed for adult human microglia compared with macaque and marmoset imaged from post-mortem
483 brain samples [56].
484
485 The most striking results produced by our transcriptomic analysis implicates vision development in
486 *SRGAP2* mutants, a function never-before reported in genetic models of *SRGAP2*. Crystallins were
487 amongst the highest upregulated genes found at 5 dpf (Figure 2B). While these genes are typically
488 associated with lens development, we observed no gross morphological defects in the lenses of stable
489 homozygous knockout larvae or adults (data not included). We did find *srgap2* to be highly expressed in
490 axonal-rich regions of the zebrafish eyes (ON and retinal GCL), in line with *Srgap2* expression observed
491 in mouse GCL [84]. Interestingly, upregulation of crystallin genes has also been reported in the retinas of
492 *Srgap2*$^{+/-}$ adult mice [28]. Alpha-crystallins are small heat-shock proteins that have been associated with
493 axonal elongation [85] and regeneration [86]. Similarly, we axonogenesis genes were upregulated in both

494 SRGAP2 mutant zebrafish and human retinal organoids, when compared to a nonhuman primate (rhesus
495 macaque). Connecting possible axonal guidance changes with vision [87], we tested visual-motor responses
496 of zebrafish larvae to abrupt light-dark changes or moving contrast stimuli [74,88] and consistently show that
497 *srgap2* knockout and *SRGAP2C*-expressing larvae have an increased response to visual cues, suggestive
498 of enhanced visual processing.
499
500 Given the presence of *srgap2*-expressing microglia in the developing zebrafish eye, we propose a model
501 where predominantly-amoeboid mutant microglia plays a role in retinal axon extension. Microglia are
502 resident macrophages in the brain that migrate into the central nervous system early in development,
503 influencing wide-ranging developmental processes such as synaptogenesis and pruning, neurogenesis, and
504 axonogenesis [89,90]. The eye is among the first regions to be colonized by microglia, at ~26–30 hpf in
505 zebrafish [59], with preferential localization to differentiating cells in the retina GCL [61] (also evident in our
506 Tg[*mpeg1.1*:GFP] lines at 3 dpf, Figure 4B). *SRGAP2*-mutant microglia, in their immature and potentially
507 activated state, could play a role in increased clearance of dead/apoptotic cells or pruning axons/synapses
508 leading to altered retinal connectivity and improved visual processing. Further, beyond impacts in the eye,
509 it is plausible that microglia mediate other brain phenotypes observed in *SRGAP2* mutant zebrafish. This
510 has recently been proposed for changes in synaptic development of cortical pyramidal neurons observed
511 in a microglia-specific *Srgap2* conditional knockout mouse model [83]. While we have yet to directly
512 connect *SRGAP2*-related microglia functions to the observed changes in Exc:Inh neuronal balance of our
513 mutant zebrafish, studies have found that microglial activation induces increased frequency of excitatory
514 synaptic events [91]. Microglia are also associated with pro- and anti-epileptic activity due to their various
515 roles in brain homeostasis and neuroinflammation [92] suggesting possible connections with seizures
516 detected in our *SRGAP2* mutants. Moving forward, generation of microglia-specific *SRGAP2* zebrafish
517 models will allow us to delineate microglia functions in retina and brain development.
518
519 While our studies using zebrafish have allowed us to query novel *SRGAP2* functions at an organismal
520 level, they also present some limitations. "Humanizing" larvae by injection of *SRGAP2C* mRNA at the
521 single-cell stage introduces the gene ubiquitously, possibly contributing to off-target phenotypes.
522 However, all published studies to date show SRGAP2C functions solely by antagonizing *srgap2,*
523 suggesting that the truncated human-specific paralog would be non-functional on its own. A strength of
524 this approach is that SRGAP2C-driven antagonism potentially produces more severe phenotypes, as it
525 avoids the genetic compensation that can occur in knockout models [81]. This might explain differences in
526 fold-change of DEGs between *srgap2* knockout and humanized models (Figure 2B), in particular across
527 vision-related genes (Note S1). Nevertheless, to avoid possible confounding factors, our conservative
528 transcriptome analysis considered only DEGs observed in both knockout and humanized *SRGAP2*
529 models. Further, because SRGAP2C was transiently introduced, we only characterized phenotypes in
530 zebrafish larvae up to 7 dpf, limiting the scope of our study to early developmental traits. Finally, the
531 structure of the zebrafish forebrain, which lacks a neocortex, limits analysis of certain processes specific
532 to mammals, such as subtle circuit changes between cortical regions observed in *SRGAP2* mouse models
533 [22]. Regardless, conservation at cellular and molecular levels has successfully enabled zebrafish models of
534 neurodevelopmental conditions impacting the cortex, such as autism and intellectual disability, across
535 hundreds of genes [93–98].
536

537 In summary, we have leveraged the advantages of viable zebrafish *SRGAP2* mutant models to investigate
538 its functional roles. Our findings are concordant with previous reports implicating *SRGAP2* in
539 neurological phenotypes and reveal novel functions in microglia and the developing eye. Combined, these
540 results provide new hypotheses regarding *SRGAP2C*-driven changes to microglia function and
541 axonogenesis in the brain and retina unique to humans, as well as improvements in visual perception,
542 opening many avenues to test in cross-species comparisons moving forward.
543

544 # Methods

545 ## Zebrafish lines and husbandry

546 NHGRI-1 wild type zebrafish lines [99] were maintained using standard protocols [100]. Animals were
547 maintained in a controlled temperature (28±0.5°C) and light (10 h dark/14 h light cycle) system with
548 UV-sterilized filtered water (Aquaneering, San Diego, CA). Feeding with rotifers (Rotigrow Nanno, Reed
549 Mariculture, Campbell, CA), brine shrimp (Artemia Brine Shrimp 90% hatch, Aquaneering, San Diego,
550 CA), and flakes (Zebrafish Select Diet, Aquaneering, San Diego, CA) and general assessment of health
551 were performed twice a day. For all assays, randomly selected pairs of adults were placed in 1 liter
552 crossing tanks (Aquaneering, San Diego, CA) in a 1 male:1 female ratio. Embryos from at least five
553 simultaneous crosses were combined. Embryos were then kept in standard Petri dishes with E3 media
554 (0.03% Instant Ocean salt in deionized water) and grown in an incubator at 28±0.5°C, and their health
555 was monitored with a dissecting microscope (Leica, Buffalo Grove, IL). Transgenic lines used for this
556 project were obtained via respective material transfer agreements and included: Tg[*vglut2a*:DsRed] [52]
557 from Dr. Hitoshi Okamoto at the RIKEN Brain Science Institute in Japan, Tg[*dlx6a*:GFP] [51], and
558 Tg[mpeg1.1:GFP] [60] from the Zebrafish International Resource Center. Zebrafish were staged as
559 previously described [33]. All animal use was approved by the Institutional Animal Care and Use
560 Committee from the Office of Animal Welfare Assurance, University of California, Davis.
561

562 ## Protein conservation

563 Coding sequences for the largest transcript for human *SRGAP2* (ENSG00000266028), *SRGAP2C*
564 (ENSG00000171943), mouse *Srgap2* (ENSMUSG00000026425), zebrafish *srgap2*
565 (ENSDARG00000032161), human *SRGAP3* (ENSG00000196220), mouse *Srgap3*
566 (ENSMUSG00000030257), zebrafish *srgap3* (ENSDARG00000060309), human *SRGAP1*
567 (ENSG00000196935), mouse *Srgap1* (ENSMUSG00000020121), zebrafish *srgap1a*
568 (ENSDARG00000007461), and zebrafish *srgap1b* (ENSDARG00000045789) were downloaded from
569 ENSEMBL [101]. Sequence alignments were performed using the R package *msa* and genetic distances
570 estimated with *seqinr*. Phylogenetic trees were created using the Unweighted Pair Group Method with
571 Arithmetic Mean (UPGMA) with the *hclust* function from the *stats* package. Protein domains were
572 extracted using the UniProtKB/Swiss-Prot database[102] and conservation estimated with the protein
573 BLAST tool [103]. Lastly, we used the *Dscript* tool[30] to predict protein-protein interactions between FBAR
574 domains in human, mouse, and zebrafish SRGAP2 orthologs.
575

576 **Protein co-immunoprecipitation**

577 HEK 293T cells were co-transfected with plasmids encoding zebrafish Srgap2-HA and human
578 SRGAP2C-GFP, or zebrafish Srgap2-HA and GFP alone, using the TurboFect™ transfection reagent
579 (Thermo Scientific, R0533) according to manufacturer's instruction. 24 h after transfection, cells were
580 lysed in 500 µl of Lysis Buffer (20 mM Tris-HCl, pH 8.0, 100 mM KCl, 5 mM $MgCl_2$, 0.2 mM EDTA,
581 10% glycerol, and 0.1% Tween 20) containing 1x protease inhibitor cocktails (Sigma-Aldrich, P8340).
582 The lysates were gently rocked back and forth for 10 min at 4°C and then cleared by centrifugation at
583 14,000 xg for 5 min at 4°C. 50 µl of the supernatant was saved as the input and the remaining 450 µl was
584 subjected to immunoprecipitation. To capture GFP and GFP fusion proteins, 30 µl of GFP-nanobody
585 conjugated agarose beads—a gift of Henry Ho and prepared as described in [104]—were washed and
586 blocked with 1 ml of 0.01% bovine serum albumin (BSA) in phosphate-buffered saline (PBS) for 1 h at
587 4°C before addition of supernatant. The supernatant-beads mix was rocked back and forth for 1 h at 4°C.
588 The beads were then washed with 1 ml of Lysis Buffer three times, 5 min each. The bound proteins were
589 eluted by incubating the beads in 25 µl of 4x Laemmli sample buffer (125 mM Tris-HCl, pH 6.8, 4%
590 sodium dodecyl sulfate, 40% glycerol, 10% 2-mercaptoethanol, and 0.01% Bromophenol blue) at 95°C
591 for 10 min. Proteins in the eluates were then resolved by 10% sodium dodecyl sulfate polyacrylamide gel
592 electrophoresis (SDS-PAGE) and transferred to a polyvinylidene difluoride (PVDF) membrane. After
593 transfer, the PVDF membrane was cut horizontally between 125- and 90-kDa protein markers and
594 blocked in Intercept™ Blocking Buffer (LI-COR, 927-60001) for 1 h at room temperature (RT). The top
595 half was then incubated with the anti-HA antibody (1:10,000 dilution, Invitrogen, 26183) and the bottom
596 half was incubated with the anti-GFP antibody (1:10,000 dilution, Proteintech, 66002-1-lg) in Intercept™
597 Blocking Buffer for 1 h at RT. After the primary antibody incubation, membranes were washed with Tris-
598 buffered saline (20 mM Tris-HCl, pH 7.6, and 150 mM NaCl) containing 0.1% Tween 20 (TBS-T) three
599 times, 5 min each, and incubated with the IRDye 800RD anti-mouse IgG secondary antibody (1:30,000
600 dilution, LI-COR, 926-68070) in Intercept™ Blocking Buffer for 1.5 h at RT. Membranes were then
601 washed with TBS-T three times, 5 min each, dried, and imaged using the Odyssey DLx imaging system
602 (LI-COR, Model 9142).
603

604 **Baseline expression of *srgap2***

605 We extract the expression of *srgap2* throughout development from public RNA-seq data that included
606 five biological replicates of pools of 12 embryos at 18 different developmental timepoints [31]. RNA-seq
607 data from embryonic and adult tissues was retrieved from a recent study [34]. Raw reads were processed
608 using *fastqc* [105], *trimmomatic* [106], and *salmon* [107] to obtain the transcripts per kilobase million (TPM)
609 values. Validation of *srgap2* temporal expression during development was performed by quantitative
610 PCR (qPCR) at selected timepoints. For this, five NHGRI-1 zebrafish pairs were crossed for each
611 timepoint and three pools of embryos (20 embryos each) collected for whole RNA extraction using the
612 RNeasy kit (Qiagen, Hilden, Germany) with gDNA eliminator columns for DNA removal. The qPCR
613 reactions were prepared following the standard protocol for the Luna kit (New England Biolabs, Ipswich,
614 MA). Oligonucleotide sequences are in Table S2.

615 **RNA *in situ* hybridization**

616 Whole embryo *in situ* hybridizations were performed as previously described [108]. Total RNA was
617 extracted from WT zebrafish embryos using Trizol and the riboprobe generated from a pBS-SK-*srgap2*
618 plasmid using a 20 µl *in vitro* transcription reaction containing ~300 ng of purified plasmid, 2 µl of 10x
619 reaction buffer (New England Biolabs, Ipswich, MA), 2 µl 0.1M DTT, 2 µl of 10x DIG labeling mix 10x
620 DIG labeling mix (Roche, Basel, Switzerland), 0.5 µl of RiboLock RNase inhibitor (Thermo Fisher,
621 Waltham, MA), 0.5 µl of RNA polymerase (T7 or T3), and nuclease-free water. Reactions were incubated
622 at 37°C for 2 h, followed by the addition of 1 µl TURBO DNase (Thermo Fisher, Waltham, MA) and 30
623 min incubation at 37°C. Reactions were stopped by adding 2 µl of STOP buffer (Promega, Madison, WI).
624 Riboprobe purification was performed with precipitation in 2 µl of 5 M LiCl and 90 µl of 100% ethanol
625 overnight at -80°C. Wild type PTU-treated 24 and 72 hpf embryos were manually dechorionated, fixed in
626 4% paraformaldehyde in 1x PBS overnight at 4°C, and treated with 10 µg/ml Proteinase K at room
627 temperature for 10 min. The hybridization medium was 65% formamide, 5x SSC, 0.1% Tween 20, 50
628 µg/ml heparin, 500 µg/ml Type X tRNA, and 9.2 mM citric acid. Embryos were pre-hybridized for 3 h in
629 a 68°C water bath, followed by hybridization with 200 ng of riboprobe in an overnight 68°C water bath.
630 After this, embryos were successively washed at 70°C with hybridization media, 2x SSC, and 0.2x SSC,
631 then with 1x PBS containing 0.1% Tween-20 (1x PBS-Tw) at room temperature. Embryos were
632 incubated for 4 h in blocking solution (2% sheep serum, 2 mg/ml BSA, 1x PBS-Tw), then overnight in
633 blocking solution and 1:5000 diluted anti-DIG antibody (Sigma Aldrich, St. Louis, MO) at 4°C. After
634 incubation, embryos were washed with 1x PBS-Tw and AP buffer (100 mM Tris pH 0.5, 100 mM NaCl,
635 5 mM $MgCl_2$, 0.1% Tween-20) at room temperature right before staining with NBT and BCIP substrates
636 (Roche, Basel, Switzerland) in AP Buffer. Images were obtained using glycerol and a stereomicroscope
637 (M165, Leica, Wetzlar, Germany) with a Leica DFC7000 T digital camera.
638

639 **Generation of *srgap2* knockout zebrafish**

640 *srgap2* was disrupted in wild type zebrafish using CRISPR/Cas9 described in previous protocols [109,110].
641 The Alt-R system from Integrated DNA Technologies (IDT, Newark, NJ) was used with the following
642 crRNA sequences: GGUCUUGCAGGAGCUGCACACGG (targeting exon 3),
643 CGCUGAUCUGGGCGAAGCGUGGG (targeting exon 4), GAGAGAGUCAGGUGAGCGAGGGG
644 (targeting exon 6), and GUCUCCUGCUAAAUUCCGAAAGG (targeting exon 2). All gRNA sequences
645 were designed using the CRISPRScan tool with the GRCz11/danRer11 genome reference[111] (sequences
646 found in Table S2). In brief, 2.5 µl of 100 µM crRNA, 2.5 µl of 100 µM tracrRNA (IDT, Newark, NJ),
647 and 5 µl of Nuclease-free Duplex Buffer (IDT, Newark, NJ) were annealed in a program of 5 min at
648 95°C, a ramp from 95°C to 50°C with a -0.1°C/s change, 10 min at 50°C, and a ramp from 50°C to 4°C
649 with a -1°C/s change. Injection mixes were prepared with 1.3 µl of SpCas9 (20 µM, New England
650 BioLabs, Ipswich, MA), 1.6 µl of annealed crRNA:tracrRNA, 2.5 µl of 4x Injection Buffer (0.2% phenol
651 red, 800 mM KCl, 4 mM $MgCl_2$, 4 mM TCEP, 120 mM HEPES, pH 7.0), and 4.6 µl of Nuclease-free
652 water. If several crRNAs were prepared in the same injection mix, equimolar quantities of each
653 crRNA:tracrRNA were included.
654

655 We microinjected one-cell-stage zebrafish embryos as described previously [110]. Briefly, needles were
656 obtained from a micropipette puller (Model P-97, Sutter Instruments) and injections were performed with

657 an air injector calibrated with a microruler (Pneumatic MPPI-2 Pressure Injector). Embryos were
658 collected and ~1 nl of injection mix injected per embryo. We used two approaches to generate *srgap2*
659 knockouts, one by injecting an injection mix including all 4 gRNAs coupled with SpCas9, and another
660 with an injection mix of the gRNA targeting exon 4 coupled with SpCas9 to create a stable line carrying
661 one specific nonsense mutation. To generate the stable *srgap2* knockout line, we outcrossed our G_0-
662 injected fish to wild type NHGRI-1 at ~1.5 months post-fertilization to obtain the G_1 heterozygous
663 generation, which was further screened by sequencing (EZ-Amplicon sequencing, Azenta, Burlington,
664 MA) a ~200 bp region that included the gRNA target site (primer sequences in Table S2). Specific alleles
665 were defined using R package *CrispRVariants*[112]. We focused on a 5-bp deletion in exon 4 referred to as
666 *srgap2*$^{tup\Delta 5}$.
667

668 **CRISPR off-target evaluation**

669 Potential off-target sites for the gRNAs were identified from previously generated CIRCLE-seq libraries
670 for each gRNA [113], following the standard protocol [114,115], and predicted using CRISPRScan [111] (Table
671 S3). Injections of each gRNA were performed as described above for subsequent DNA extraction at 5 dpf
672 of injected and non-injected batch-sibling controls, PCR amplification of the top ten off-target sites from
673 each approach (CIRCLE-seq and CRISPRScan), followed by Sanger sequencing (Azenta, Burlington,
674 MA).
675

676 **Injection of human mRNA in zebrafish**

677 Temporal expression of *SRGAP2C* mRNA in zebrafish was performed similarly to previously described
678 protocols [116,117]. The mammalian expression vector pEF-DEST51 containing *SRGAP2C* was used to
679 produce 5'-capped mRNA using the MEGAshortscript T7 transcription kit (Thermo Fisher, Waltham,
680 MA) following the manufacturer's guidelines with a 3.5 h 56°C incubation with T7 polymerase. mRNA
681 was then purified with the MEGAclear transcription clean-up kit (Thermo Fisher, Waltham, MA),
682 measured using a Qubit (Thermo Fisher, Waltham, MA) and evaluated for integrity by 2% agarose gel
683 electrophoresis. The injection mix contained 100 ng/µl of mRNA, 4x Injection Buffer (0.2% phenol red,
684 800 mM KCl, 4 mM $MgCl_2$, 4 mM TCEP, 120 mM HEPES, pH 7.0), and nuclease-free water. As
685 described above, one-cell stage zebrafish embryos were injected with ~1 nl of the injection mix and kept
686 at 28°C until needed.
687

688 **Morphometric measurements**

689 High-throughput imaging of zebrafish larvae was performed using the VAST BioImager system (Union
690 Biometrica, Holliston, MA) as previously described [113,118]. In brief, 5 dpf larvae were placed in a rotating
691 600 µm capillary coupled with a camera, allowing for the automatic acquisition of images from all four
692 sides. Images were automatically processed using FishInspector v1.7 [119] to identify and extract
693 morphological shapes, which were then analyzed with the *TableCreator* tool. Images of dead or truncated
694 larvae were discarded. In total, we measured the central line, head area, Euclidean distance between the
695 eyes, and the head-trunk angle across 331 larvae. As no significant differences in measurements of any
696 feature were observed between our controls (uninjected NHGRI-1 wild type larvae, wild type larvae from

697 the stable *srgap2* knockout line, and wild type NHGRI-1 larvae injected with SpCas9 coupled with a
698 scrambled gRNA; all pairwise t-tests p-values > 0.05, complete results in Table S26), we merged these
699 larvae into a single control group.
700

701 **Bulk RNA-seq**

702 For stable *srgap2* knockout larvae, a minimum of 3 different $srgap2^{+}/srgap2^{tup\Delta 5}$ x $srgap2^{+}/srgap2^{tup\Delta 5}$
703 crosses were set embryos were pooled in the batches, and larvae were kept at 28°C until 5 dpf when they
704 were flash frozen and placed in RNA later (Thermo Fisher, Waltham, MA). Tails were then cut off each
705 larva for genotyping via high resolution melt (HRM) curve in a CFX 96 Real-Time System qPCR
706 machine (BioRad). HRM mix included 5 µl DreamTaq DNA polymerase (Thermo Fisher, Waltham,
707 MA), 0.5 µl of each primer at 10 µM, 1 µl of 1x SYBR green (Thermo Fisher, Waltham, MA) and 2 µl of
708 nuclease-free water. In parallel, wild type crosses were set and one-cell stage embryos were injected with
709 human *SRGAP2C* mRNA or the G_0 knockout. Injections were performed as previously described, using
710 ~1 nl of the injection mix. For all samples, the heads of five larvae were pooled together and RNA
711 extracted using the RNeasy kit (Qiagen, Hilden, Germany) with gDNA eliminator columns for DNA
712 removal. In total, three samples per group were harvested. Total RNA was then submitted for RNA-seq
713 using poly-A selection and standard library preparation for Illumina sequencing (Genewiz, South
714 Plainfield, NJ).
715
716 In a similar manner, 3'-tagged RNA-seq was performed for gene expression evaluations at earlier
717 timepoints. *srgap2* knockouts (stable and pooled), *SRGAP2C*-mRNA injected, and controls were co-
718 injected with SpCas9 and a scrambled gRNA were obtained as previously described. Embryos from each
719 group were collected at 24 hpf (n= 20 larvae per replicate), 48 hpf (n= 10 per sample), and 72 hpf (n= 10
720 per sample) for flash freezing and incubation in RNAlater (Thermo Fisher, Waltham, MA) at -20°C,
721 completing three replicates per group per timepoint. Once all samples were collected, RNA was extracted
722 from dissected heads using the RNeasy kit (Qiagen, Hilden, Germany). RNA samples were submitted to
723 the UC Davis DNA Technologies Core (Davis, CA) for library preparation and sequencing.
724
725 All raw RNA-seq reads were trimmed using *trim-galore* and then mapped to the published zebrafish
726 optimized transcriptome [120] using *STAR* [121]. Gene-level counts were obtained with *HTseq* [122]. Overall,
727 samples exhibited high correlations in gene counts for both the RNA-seq (mean Spearman ρ= 0.97, range
728 0.95-0.99) and 3'-tagged RNA-seq (mean Spearman ρ= 0.88, range 0.85-0.93). Differentially expressed
729 genes were obtained with *DESeq2* [123] using WT samples from the stable line as controls for the stable
730 knockouts, and injection controls (SpCas9 coupled with a scrambled gRNA) for the G_0-knockouts and
731 *SRGAP2C*-injected embryos. All enrichment tests of gene groups in specific biological pathways were
732 performed using *clusterProfiler* [124] with the background genes including all expressed genes in each
733 dataset (e.g., all genes expressed in microglia cells).
734

735 **Single-cell RNA-seq**

736 Embryos were incubated at 28°C. At 3 dpf, the heads of larvae from each group were dissected after
737 euthanasia in cold tricaine (0.025%), pooling 30 heads together per sample (n= three samples per group).

Cell dissociation was performed immediately afterward, using previous protocols as reference [125,126], with two washes in 1 ml cold 1x PBS on ice and immediate incubation at 28°C for 15 min in a preheated dissociation mix that included 480 µl of 0.25% trypsin-EDTA (Thermo Fisher, Waltham, MA) and 20 µl of collagenase P (100 mg/ml, Sigma-Aldrich, St. Louis, MO). Every 5 min all samples were gently pipetted using a cut P1000 tip. After 15 min, 800 µl stop solution (DMEM with 10% FBS) was added to each sample and immediately centrifuged at 700 g in 4°C for 5 min. The supernatant was discarded and cells were resuspended in cold 1x PBS for another 5 min centrifugation at 700 g in 4°C. After this, the supernatant was discarded and cells were resuspended in 800 µl suspension solution (DMEM with 10% FBS) and filtered through a Flowmi 40 µm cell strainer (Sigma Aldrich, St. Louis, MO) into a low-bind DNA tube (Eppendorf, Hamburg, Germany). Intact cells were counted using a Countess II (Thermo Fisher, Waltham, MA) and cell viability was confirmed to be >65%. Cell fixation and library preparation were then performed with the Parse Biosciences Fixation and Single Cell Whole Transcriptome kit v1.3.0 (Parse Biosciences, Seattle, WA), following the manufacturer's instructions. A total of 12,500 cells per well were loaded into the barcoding plate and two resulting sub-libraries were sequenced in a NovaSeq 6000 platform.

Raw FASTQ scRNA-seq reads were processed using the Parse Biosciences processing pipeline v0.9.3 and the optimized zebrafish transcriptome [120] to obtain the gene x cell matrix files per sample. These matrices were processed into Seurat objects using *Seurat* v4 [127]. Quality control filtering included feature counts above 200 and below two standard deviations from the mean (5727 features), less than 5% mitochondrial or ribosomal percentages, and doublets removal with *DoubletFinder* [128] with a 4% expected doublets for the SPLiT-seq method [129]. Data for an average of 2391±250 cells per sample were obtained (full sample information in Table S9), which were normalized using *SCTransform* with the top 5,000 variable genes and regressing for mitochondrial and ribosomal percentages. Samples were then integrated using a canonical correlation analysis reduction [127] and nearest-neighbor graphs constructed using the first 15 principal components with the *FindNeighbors* function. Hierarchical clustering was performed with the Euclidean distance between principal components embeddings (tree cut at k=40) and cluster marker genes obtained with *PrepSCTFindMarkers* and *FindAllMarkers* using the Wilcoxon test option (parameters: *logfc.threshold*= 0.1, *min.pct*= 0.1, *return.thresh*= 0.01, *only.pos*= TRUE), which were further detailed using zebrafish brain atlases [44,45] and the ZFIN database [130]. For the pseudo-bulk analysis, count data was aggregated using *AggregateExpression* and the differential expression test between cell types of different genotypes (e.g., mutant microglia cells vs control microglia cells) performed with the MAST test option [131] (parameters: *logfc.threshold*= 0.02, *min.pct*= 0.1, *only.pos*= FALSE). Several functions from *scCustomize* [132] were used for making plots.

Knockout models exhibited significantly reduced *srgap2* expression (ANOVA genotype effect *p*-value= 3.15×10^{-4}, Hom *p*-value= 5.80×10^{-4}, G_0-knockouts *p*-value= 0.011, Table S9), while no reduction was observed in the *SRGAP2C*-injected samples (*SRGAP2C*-humanized *p*-value= 0.992, Table S9), consistent with observations from our quantitative RT-PCR results (Figure S1A). Bulk RNA-seq showed high correlation with single-cell pseudo-bulk gene counts of the same genotype at 3 dpf (average Spearman ρ across genotypes= 0.76±0.03, all *p*-values < 2.2×10^{-16}).

780 **Quantification of neuronal populations**

781 *SRGAP2* models and controls were created as previously described (above) in a Tg[*vglut2*:DsRed] x
782 Tg[*d1x6a*:GFP] background. Embryos were kept at 28°C until 3 dpf, when larvae were anesthetized in
783 tricaine (0.0125%) and embedded in 1% low-melting agarose (n= 6–7 per group). These embryos were
784 imaged using a spinning disk confocal microscope system (Dragonfly, Andor Technology, Belfast,
785 United Kingdom) housed inside an incubator (Okolab, Pozzouli, Italy) with Leica 10x and 20x objectives
786 and an iXon camera (Andor Technology, Belfast, United Kingdom). All imaging was performed using Z-
787 stacking of 10 µm slices starting in the dorsal-most part going ventrally until no fish was detected. Image
788 processing was done using Fiji [133] by generating hyperstacks with maximum intensity projections and
789 quantifying all areas either GFP or DsRed positive.
790

791 **Motion-tracking activity screen**

792 We performed motion-tracking recordings of 4 dpf larvae using the Zebrabox system with a camera
793 acquisition speed of 30 frames per second (ViewPoint, Montreal, Canada). Larvae were placed in a 96-
794 well plate with 150 µl of E3 media with 0 mM or 2.5 mM pentylenetetrazol (PTZ, #P6500, Sigma-
795 Aldrich, St. Louis, MO) and their movement was recorded for 15 min. A published MATLAB script was
796 used to extract high-speed movement (>28 mm/s) events from data extracted in 1 s bins [55] and compared
797 across groups.
798

799 **Electrophysiology**

800 Larvae (n= 20–30) at 4 dpf were randomly selected for local field potential (LPF) recordings, as
801 previously described [55]. Briefly, larvae were exposed to pancuronium (300 µM) and immobilized in 2%
802 low-melting agarose in a vertical slice perfusion chamber (Siskiyou Corporation, #PC-V, Grant Pass,
803 OR). These chambers were then placed on an upright microscope (Olympus BX-51W, Lausanne,
804 Switzerland) and monitored with a Zeiss Axiocam digital camera. 15 min LFP recordings were obtained
805 by placing a single-glass microelectrode (WPI glass #TW150 F-3) with a ~1 µm tip diameter in the optic
806 tectum under visual guidance. The voltage signals were filtered at 1 kHz and digitized at 10 kHz using
807 Digidata 1320 A/D interface (Molecular Devices, San Jose, CA). All recordings were coded and scored
808 independently by three researchers using Clampfit software (Molecular Devices, San Jose, CA) to obtain
809 the final LFP score per group.
810

811 **Histology and immunostaining**

812 We evaluated the general morphology of the eye in 5 dpf larvae and performed immunohistochemistry
813 using anti-Pax6 antibodies (Thermo Fisher, Waltham, MA) to label the amacrine and retinal ganglion
814 cells in the eyes. In brief, 10 µm sections for each group were collected using a cryostat microtome
815 (Leica, Wetzlar, Germany) and placed on slides at -80°C. Slides were then brought to room temperature
816 and washed with 1 ml 1x PBS for 5 min, followed by incubation with blocking buffer (4% milk/TST
817 buffer) for 1 h. Then, the blocking buffer was removed, and slides were incubated with anti-Pax6
818 antibodies in blocking buffer overnight at 4°C. Incubation with a secondary anti-mouse antibody (Thermo

819 Fisher, Waltham, MA) was performed for 1 h after a wash with fresh blocking buffer. Images were
820 obtained using a confocal microscope (Olympus, Lausanne, Switzerland). Additionally, cryosections (10
821 µm) from each group were stained with hematoxylin and eosin (H&E) and mounted in Permount.
822

823 **Visual-motor response assays**

824 We performed visual-motor response tests on 5 dpf larvae in a 96-well plate with 150 µl E3 media per
825 well (n= 24 per group). Using the Zebrabox system (ViewPoint, Montreal, Canada), we exposed larvae to
826 a protocol consisting of 10 min dark adaptation followed by bright light (100 lumens) and recorded their
827 movement responses. Movement data were exported in 1 s bins for comparisons across groups in the 20 s
828 prior and post dark-to-light change. Additionally, we performed optomotor response (OMR) tests
829 following a protocol that uses a monitor to display a video with 30 s periods of contrasting stripes moving
830 at 1.04 rad/s separated by 20s intervals [73]. We placed 4 larvae per group in a standard Petri dish and
831 exposed them to 5 cycles of the recording, with 3 replicates per group (n= 12 larval measurements per
832 group). In separate experiments, video recordings were paused during every cycle, after exactly 10 s
833 (halfway through the video) and the number of larvae with rostral ends oriented in the direction of the
834 moving stripes was recorded, giving the "OMR positive" response. The quantification was performed
835 blind to genotype.
836

837 **Microglia morphology and abundance**

838 One-cell stage larvae from a Tg[*mpeg1.1*:GFP] cross were microinjected as described above to generate
839 *srgap2* G_0-knockouts, *SRGAP2C*-injected, and scrambled gRNA-injected controls. At 3 and 7 dpf, larvae
840 were anesthetized with MS-222 (0.175 mg/ml in E3 media), embedded in 1% low-melt agar, and
841 immediately imaged with a spinning disk confocal microscope system fitted with a 63X lens (Dragonfly,
842 Andor Technology, Belfast, United Kingdom) as described above. Sphericity was obtained as described
843 [62,134] using the Imaris software (Bitplane, Switzerland) and creating 3D surface reconstructions per cell.
844 Parameters were consistent across samples, including a smooth selection of 0.191µm and thresholding of
845 absolute intensity. A total of one to five microglial cells were imaged from three to four larvae per
846 genotype per timepoint. Microglial cells were quantified according to an established protocol [59,135]. 3dpf
847 larvae were incubated in E3 media containing 2.5 µg/ml neutral red at 28.5°C for 3 hr, followed by two
848 water changes and imaged immediately after using a stereoscope (M165, Leica, Wetzlar, Germany) with
849 a Leica DFC7000 T digital camera.
850

851 **Human and non-human primates scRNA-seq**

852 scRNA-seq data from human retinal organoids [68] (43,857 cells), human donors [70] (183,808 cells),
853 macaque retinal organoids [69] (19,894 cells), macaque donors [70] (165,681 cells), and prefrontal cortex data
854 from humans and non-human primates[66] (171,997 human cells, 158,099 chimpanzee cells, 131,032
855 macaque cells, 149,468 marmoset cells) were downloaded as preprocessed objects. Retinal datasets were
856 integrated using the LIGER method for cross-species analyses [136] followed by joint matrix factorization
857 with *optimizeALS* using a lambda of 5, a convergence threshold of $1x10^{-10}$, and a k of 30. Differentially
858 expressed genes were obtained with *getFactorMarkers*, using the human data as reference. Enrichment of
859 genes in biological pathways was performed using *clusterProfiler* [124]. For the prefrontal cortex data [66], we

obtained differentially expressed genes with the *FindMarkers* function from Seurat v4.0 [127] using the Wilcoxon test option. Microglial cells defined in the prefrontal cortex [66] and the middle temporal gyrus [137] were gathered totaling 30,918 cells (prefrontal cortex: human= 7,556, chimpanzee= 5,748, macaque= 8,058, marmoset= 4,626; middle temporal gyrus: human= 1,263, chimpanzee= 252, macaque= 942, marmoset= 2473) and their expression aggregated using *AggregateExpression* from Seurat [127], grouping by organism to obtain a gene by organism pseudo count table. Differential gene expression between species was then performed with *DESeq2* [123] and overrepresentation tests in GO terms with DAVID [138].

Statistical analysis

All statistical analyses were performed in R version 4.0.2, and all scripts are available in the GitHub repository https://github.com/mydennislab/public_data/ (zenodo pending). Comparisons between groups were performed using two-tailed Student's t-tests, Mann-Whitney U-tests, Analysis of Variance (ANOVA) or nonparametric Dunn's tests, depending on the normality of the data assessed using the Shapiro-Wilk test. All analyses across experimental batches included *batch* as a factor in the model to control for biases caused by inter-batch differences. Fisher's exact tests were used for testing significant overlaps between gene lists. All mean values reported include their standard deviation unless otherwise noted. Significance thresholds were defined with an alpha of 0.05 and the proper corrections for multiple comparisons defined in the text. All gene ontology enrichment tests were performed using solely the expressed genes as the background gene list.

Data availability

GEO numbers of deposited data pending: bulk RNA-seq, scRNA-seq

Acknowledgements

We thank Kyle Burbach, Daisy Castillo, Aarthi Sekar, Dr. Alexandra Colón-Rodríguez, and Eva Ferino for their support in helping to generate and maintain the *srgap2* stable knockout line. We also thank Dr. Colin Shew, Jennielee Mia, Xueer Jiang, and Ingrid Brust-Mascher for technical support in computational and imaging analyses. We thank Drs. Bruce Draper, Kristen Kwan, Heather Mefford, Anna La Torre, Ala Moshiri, Nick Marsh-Armstrong, and Paul FitzGerald for many fruitful discussions, ideas, reagents, and advice. We thank the Cell Biology and Human Anatomy Department at UC Davis School of Medicine for the support to use multiple pieces of imaging equipment. We also thank Dr. Elizabeth Haswell, as well as Aidan Baraban and Gabriana La for significant edits to the manuscript. This work was supported, in part, by the U.S. National Institutes of Health (NIH) grants from the Office of the Director and National Institute of Mental Health (DP2MH119424 and R01MH132818 to M.Y.D.), UC Davis MIND Institute Intellectual and Developmental Disabilities Research Center pilot grant (U54 HD079125 to M.Y.D.), NIH National Institute of General Medical Sciences (NIGMS) (R01GM144435 to L.-E.J.), NIH National Institute of Neurological Disorders and Stroke (R01NS096976 and R01NS103139 to S.C.B, and R01NS109176 to S.S.). NKH is supported by an NIH NIGMS UC Davis eMCDB T32 (T32GM153586), and a UC Davis Graduate Research Award (J.M.U-S.).

900 **References**

901 1. Pääbo, S. (2014). The Human Condition—A Molecular Approach. Preprint,
902 https://doi.org/10.1016/j.cell.2013.12.036 https://doi.org/10.1016/j.cell.2013.12.036.

903 2. Varki, A., and Altheide, T.K. (2005). Comparing the human and chimpanzee genomes: searching for
904 needles in a haystack. Genome Res. *15*, 1746–1758.

905 3. Ohno, S. (1970). Evolution by Gene Duplication.

906 4. Zhang, J. (2003). Evolution by gene duplication: an update. Trends Ecol. Evol. *18*, 292–298.

907 5. Bailey, J.A., Yavor, A.M., Massa, H.F., Trask, B.J., and Eichler, E.E. (2001). Segmental
908 duplications: organization and impact within the current human genome project assembly. Genome
909 Res. *11*, 1005–1017.

910 6. Dennis, M.Y., Harshman, L., Nelson, B.J., Penn, O., Cantsilieris, S., Huddleston, J., Antonacci, F.,
911 Penewit, K., Denman, L., Raja, A., et al. (2017). The evolution and population diversity of human-
912 specific segmental duplications. Nat Ecol Evol *1*, 69.

913 7. Bailey, J.A., Gu, Z., Clark, R.A., Reinert, K., Samonte, R.V., Schwartz, S., Adams, M.D., Myers,
914 E.W., Li, P.W., and Eichler, E.E. (2002). Recent segmental duplications in the human genome.
915 Science *297*, 1003–1007.

916 8. Conrad, B., and Antonarakis, S.E. (2007). Gene duplication: a drive for phenotypic diversity and
917 cause of human disease. Annu. Rev. Genomics Hum. Genet. *8*, 17–35.

918 9. Sudmant, P.H., Huddleston, J., Catacchio, C.R., Malig, M., Hillier, L.W., Baker, C., Mohajeri, K.,
919 Kondova, I., Bontrop, R.E., Persengiev, S., et al. (2013). Evolution and diversity of copy number
920 variation in the great ape lineage. Genome Res. *23*, 1373–1382.

921 10. Marques-Bonet, T., Kidd, J.M., Ventura, M., Graves, T.A., Cheng, Z., Hillier, L.W., Jiang, Z.,
922 Baker, C., Malfavon-Borja, R., Fulton, L.A., et al. (2009). A burst of segmental duplications in the
923 genome of the African great ape ancestor. Nature *457*, 877–881.

924 11. Marques-Bonet, T., Girirajan, S., and Eichler, E.E. (2009). The origins and impact of primate
925 segmental duplications. Trends Genet. *25*, 443–454.

926 12. Sudmant, P.H., Kitzman, J.O., Antonacci, F., Alkan, C., Malig, M., Tsalenko, A., Sampas, N.,
927 Bruhn, L., Shendure, J., 1000 Genomes Project, et al. (2010). Diversity of human copy number
928 variation and multicopy genes. Science *330*, 641–646.

929 13. Soto, D.C., Uribe-Salazar, J.M., Shew, C.J., Sekar, A., McGinty, S.P., and Dennis, M.Y. (2023).
930 Genomic structural variation: A complex but important driver of human evolution. Am J Biol
931 Anthropol *181 Suppl 76*, 118–144.

932 14. Guerrier, S., Coutinho-Budd, J., Sassa, T., Gresset, A., Jordan, N.V., Chen, K., Jin, W.-L., Frost, A.,
933 and Polleux, F. (2009). The F-BAR domain of srGAP2 induces membrane protrusions required for
934 neuronal migration and morphogenesis. Cell *138*, 990–1004.

935 15. Fiddes, I.T., Lodewijk, G.A., Mooring, M., Bosworth, C.M., Ewing, A.D., Mantalas, G.L., Novak,
936 A.M., van den Bout, A., Bishara, A., Rosenkrantz, J.L., et al. (2018). Human-Specific NOTCH2NL
937 Genes Affect Notch Signaling and Cortical Neurogenesis. Cell *173*, 1356–1369.e22.

938 16. Florio, M., Albert, M., Taverna, E., Namba, T., Brandl, H., Lewitus, E., Haffner, C., Sykes, A.,
939 Wong, F.K., Peters, J., et al. (2015). Human-specific gene ARHGAP11B promotes basal progenitor
940 amplification and neocortex expansion. Science *347*, 1465–1470.

941 17. Ju, X.-C., Hou, Q.-Q., Sheng, A.-L., Wu, K.-Y., Zhou, Y., Jin, Y., Wen, T., Yang, Z., Wang, X., and
942 Luo, Z.-G. (2016). The hominoid-specific gene TBC1D3 promotes generation of basal neural
943 progenitors and induces cortical folding in mice. Elife *5*. https://doi.org/10.7554/eLife.18197.

944 18. Fossati, M., Pizzarelli, R., Schmidt, E.R., Kupferman, J.V., Stroebel, D., Polleux, F., and Charrier,
945 C. (2016). SRGAP2 and Its Human-Specific Paralog Co-Regulate the Development of Excitatory
946 and Inhibitory Synapses. Neuron *91*, 356–369.

947 19. Libé-Philippot, B., Lejeune, A., Wierda, K., Vlaeminck, I., Beckers, S., Gaspariunaite, V., Bilheu,
948 A., Nyitrai, H., Vennekens, K.M., Bird, T.W., et al. (2022). LRRC37B is a species-specific regulator
949 of voltage-gated channels and excitability in human cortical neurons. bioRxiv, 2022.12.21.521423.
950 https://doi.org/10.1101/2022.12.21.521423.

951 20. Van Heurck, R., Bonnefont, J., Wojno, M., Suzuki, I.K., Velez-Bravo, F.D., Erkol, E., Nguyen,
952 D.T., Herpoel, A., Bilheu, A., Beckers, S., et al. (2023). CROCCP2 acts as a human-specific
953 modifier of cilia dynamics and mTOR signaling to promote expansion of cortical progenitors.
954 Neuron *111*, 65–80.e6.

955 21. Charrier, C., Joshi, K., Coutinho-Budd, J., Kim, J.-E., Lambert, N., de Marchena, J., Jin, W.-L.,
956 Vanderhaeghen, P., Ghosh, A., Sassa, T., et al. (2012). Inhibition of SRGAP2 function by its human-
957 specific paralogs induces neoteny during spine maturation. Cell *149*, 923–935.

958 22. Schmidt, E.R.E., Zhao, H.T., Park, J.M., Dipoppa, M., Monsalve-Mercado, M.M., Dahan, J.B.,
959 Rodgers, C.C., Lejeune, A., Hillman, E.M.C., Miller, K.D., et al. (2021). A human-specific modifier
960 of cortical connectivity and circuit function. Nature *599*, 640–644.

961 23. Dennis, M.Y., Nuttle, X., Sudmant, P.H., Antonacci, F., Graves, T.A., Nefedov, M., Rosenfeld, J.A.,
962 Sajjadian, S., Malig, M., Kotkiewicz, H., et al. (2012). Evolution of human-specific neural SRGAP2
963 genes by incomplete segmental duplication. Cell *149*, 912–922.

964 24. Schmidt, E.R.E., Kupferman, J.V., and Stackmann, M. (2019). The human-specific paralogs
965 SRGAP2B and SRGAP2C differentially modulate SRGAP2A-dependent synaptic development.
966 Scientific Reports *9*. https://doi.org/10.1101/596940.

967 25. Dennis, M.Y., and Eichler, E.E. (2016). Human adaptation and evolution by segmental duplication.
968 Curr. Opin. Genet. Dev. *41*, 44–52.

969 26. Sporny, M., Guez-Haddad, J., Kreusch, A., Shakartzi, S., Neznansky, A., Cross, A., Isupov, M.N.,
970 Qualmann, B., Kessels, M.M., and Opatowsky, Y. (2017). Structural History of Human SRGAP2
971 Proteins. Mol. Biol. Evol. *34*, 1463–1478.

972 27. Pollen, A.A., Kilik, U., Lowe, C.B., and Camp, J.G. (2023). Human-specific genetics: new tools to
973 explore the molecular and cellular basis of human evolution. Nat. Rev. Genet. *24*, 687–711.

974 28. Gan, Y.-J., Cao, Y., Zhang, Z.-H., Zhang, J., Chen, G., Dong, L.-Q., Li, T., Shen, M.-X., Qu, J., and
975 Chi, Z.-L. (2023). Srgap2 suppression ameliorates retinal ganglion cell degeneration in mice. Neural
976 Regeneration Res. *18*, 2307.

977 29. Saitsu, H., Osaka, H., Sugiyama, S., Kurosawa, K., Mizuguchi, T., Nishiyama, K., Nishimura, A.,
978 Tsurusaki, Y., Doi, H., Miyake, N., et al. (2012). Early infantile epileptic encephalopathy associated

979 with the disrupted gene encoding Slit-Robo Rho GTPase activating protein 2 (SRGAP2). Am. J.
980 Med. Genet. A *158A*, 199–205.

981 30. Sledzieski, S., Singh, R., Cowen, L., and Berger, B. (2021). D-SCRIPT translates genome to
982 phenome with sequence-based, structure-aware, genome-scale predictions of protein-protein
983 interactions. Cell Syst *12*, 969–982.e6.

984 31. White, R.J., Collins, J.E., Sealy, I.M., Wali, N., Dooley, C.M., Digby, Z., Stemple, D.L., Murphy,
985 D.N., Billis, K., Hourlier, T., et al. (2017). A high-resolution mRNA expression time course of
986 embryonic development in zebrafish. Elife *6*. https://doi.org/10.7554/eLife.30860.

987 32. Schwarzer, S., Asokan, N., Bludau, O., Chae, J., Kuscha, V., Kaslin, J., and Hans, S. (2020).
988 Neurogenesis in the inner ear: the zebrafish statoacoustic ganglion provides new neurons from a
989 Neurod/Nestin-positive progenitor pool well into adulthood. Development *147*.
990 https://doi.org/10.1242/dev.176750.

991 33. Kimmel, C.B., Ballard, W.W., Kimmel, S.R., Ullmann, B., and Schilling, T.F. (1995). Stages of
992 embryonic development of the zebrafish. Dev. Dyn. *203*, 253–310.

993 34. Yang, H., Luan, Y., Liu, T., Lee, H.J., Fang, L., Wang, Y., Wang, X., Zhang, B., Jin, Q., Ang, K.C.,
994 et al. (2020). A map of cis-regulatory elements and 3D genome structures in zebrafish. Nature *588*,
995 337–343.

996 35. Varshney, G.K., Pei, W., LaFave, M.C., Idol, J., Xu, L., Gallardo, V., Carrington, B., Bishop, K.,
997 Jones, M., Li, M., et al. (2015). High-throughput gene targeting and phenotyping in zebrafish using
998 CRISPR/Cas9. Genome Res. *25*, 1030–1042.

999 36. Varshney, G.K., Carrington, B., Pei, W., Bishop, K., Chen, Z., Fan, C., Xu, L., Jones, M., LaFave,
1000 M.C., Ledin, J., et al. (2016). A high-throughput functional genomics workflow based on
1001 CRISPR/Cas9-mediated targeted mutagenesis in zebrafish. Nat. Protoc. *11*, 2357–2375.

1002 37. Thyme, S.B., Pieper, L.M., Li, E.H., Pandey, S., Wang, Y., Morris, N.S., Sha, C., Choi, J.W.,
1003 Herrera, K.J., Soucy, E.R., et al. (2019). Phenotypic Landscape of Schizophrenia-Associated Genes
1004 Defines Candidates and Their Shared Functions. Cell *177*, 478–491.e20.

1005 38. Shah, A.N., Davey, C.F., Whitebirch, A.C., Miller, A.C., and Moens, C.B. (2015). Rapid reverse
1006 genetic screening using CRISPR in zebrafish. Nat. Methods *12*, 535–540.

1007 39. Kroll, F., Powell, G.T., Ghosh, M., Gestri, G., Antinucci, P., Hearn, T.J., Tunbak, H., Lim, S.,
1008 Dennis, H.W., Fernandez, J.M., et al. (2021). A simple and effective F0 knockout method for rapid
1009 screening of behaviour and other complex phenotypes. Elife *10*. https://doi.org/10.7554/eLife.59683.

1010 40. Wu, R.S., Lam, I.I., Clay, H., Duong, D.N., Deo, R.C., and Coughlin, S.R. (2018). A Rapid Method
1011 for Directed Gene Knockout for Screening in G0 Zebrafish. Dev. Cell *46*, 112–125.e4.

1012 41. Romo, L., Gold, N.B., and Walker, M.A. (2024). Endocrine features of primary mitochondrial
1013 diseases. Curr. Opin. Endocrinol. Diabetes Obes. *31*, 34–42.

1014 42. Marcó de la Cruz, B., Campos, J., Molinaro, A., Xie, X., Jin, G., Wei, Z., Acuna, C., and Sterky,
1015 F.H. (2024). Liprin-α proteins are master regulators of human presynapse assembly. Nat. Neurosci.
1016 *27*, 629–642.

1017 43. Rosenberg, A.B., Roco, C.M., Muscat, R.A., Kuchina, A., Sample, P., Yao, Z., Graybuck, L.T.,
1018 Peeler, D.J., Mukherjee, S., Chen, W., et al. (2018). Single-cell profiling of the developing mouse

1019 brain and spinal cord with split-pool barcoding. Science *360*, 176–182.

1020 44. Raj, B., Farrell, J.A., Liu, J., El Kholtei, J., Carte, A.N., Navajas Acedo, J., Du, L.Y., McKenna, A.,
1021 Relić, Đ., Leslie, J.M., et al. (2020). Emergence of Neuronal Diversity during Vertebrate Brain
1022 Development. Neuron *108*, 1058–1074.e6.

1023 45. Zhang, H., Wang, H., Shen, X., Jia, X., Yu, S., Qiu, X., Wang, Y., Du, J., Yan, J., and He, J. (2021).
1024 The landscape of regulatory genes in brain-wide neuronal phenotypes of a vertebrate brain. Elife *10*.
1025 https://doi.org/10.7554/eLife.68224.

1026 46. Cowan, C.A., Yokoyama, N., Bianchi, L.M., Henkemeyer, M., and Fritzsch, B. (2000). EphB2
1027 guides axons at the midline and is necessary for normal vestibular function. Neuron *26*, 417–430.

1028 47. Henkemeyer, M., Orioli, D., Henderson, J.T., Saxton, T.M., Roder, J., Pawson, T., and Klein, R.
1029 (1996). Nuk controls pathfinding of commissural axons in the mammalian central nervous system.
1030 Cell *86*, 35–46.

1031 48. Cheng, R.-K., Jesuthasan, S.J., and Penney, T.B. (2014). Zebrafish forebrain and temporal
1032 conditioning. Philos. Trans. R. Soc. Lond. B Biol. Sci. *369*. https://doi.org/10.1098/rstb.2012.0462.

1033 49. Burgess, H.A., and Burton, E.A. (2023). A Critical Review of Zebrafish Neurological Disease
1034 Models−1. The Premise: Neuroanatomical, Cellular and Genetic Homology and Experimental
1035 Tractability. Oxford Open Neuroscience *2*. https://doi.org/10.1093/oons/kvac018.

1036 50. Martin, A., Babbitt, A., Pickens, A.G., Pickett, B.E., Hill, J.T., and Suli, A. (2022). Single-Cell RNA
1037 Sequencing Characterizes the Molecular Heterogeneity of the Larval Zebrafish Optic Tectum. Front.
1038 Mol. Neurosci. *15*, 818007.

1039 51. Yu, M., Xi, Y., Pollack, J., Debiais-Thibaud, M., Macdonald, R.B., and Ekker, M. (2011). Activity
1040 of dlx5a/dlx6a regulatory elements during zebrafish GABAergic neuron development. Int. J. Dev.
1041 Neurosci. *29*, 681–691.

1042 52. Satou, C., Kimura, Y., and Higashijima, S.-I. (2012). Generation of multiple classes of V0 neurons
1043 in zebrafish spinal cord: progenitor heterogeneity and temporal control of neuronal diversity. J.
1044 Neurosci. *32*, 1771–1783.

1045 53. Hoffman, E.J., Turner, K.J., Fernandez, J.M., Cifuentes, D., Ghosh, M., Ijaz, S., Jain, R.A., Kubo, F.,
1046 Bill, B.R., Baier, H., et al. (2016). Estrogens Suppress a Behavioral Phenotype in Zebrafish Mutants
1047 of the Autism Risk Gene, CNTNAP2. Neuron *89*, 725–733.

1048 54. Brenet, A., Hassan-Abdi, R., Somkhit, J., Yanicostas, C., and Soussi-Yanicostas, N. (2019).
1049 Defective excitatory/inhibitory synaptic balance and increased neuron apoptosis in a zebrafish model
1050 of Dravet syndrome. Preprint, https://doi.org/10.1101/781393 https://doi.org/10.1101/781393.

1051 55. Griffin, A., Carpenter, C., Liu, J., Paterno, R., Grone, B., Hamling, K., Moog, M., Dinday, M.T.,
1052 Figueroa, F., Anvar, M., et al. (2021). Phenotypic analysis of catastrophic childhood epilepsy genes.
1053 Commun Biol *4*, 680.

1054 56. Geirsdottir, L., David, E., Keren-Shaul, H., Weiner, A., Bohlen, S.C., Neuber, J., Balic, A., Giladi,
1055 A., Sheban, F., Dutertre, C.-A., et al. (2019). Cross-Species Single-Cell Analysis Reveals
1056 Divergence of the Primate Microglia Program. Cell *179*, 1609–1622.e16.

1057 57. Coutinho-Budd, J., Ghukasyan, V., Zylka, M.J., and Polleux, F. (2012). The F-BAR domains from
1058 srGAP1, srGAP2 and srGAP3 regulate membrane deformation differently. J. Cell Sci. *125*, 3390–

1059 3401.

1060 58. Lucas, B., and Hardin, J. (2017). Mind the (sr)GAP - roles of Slit-Robo GAPs in neurons, brains and
1061 beyond. J. Cell Sci. *130*, 3965–3974.

1062 59. Herbomel, P., Thisse, B., and Thisse, C. (2001). Zebrafish early macrophages colonize cephalic
1063 mesenchyme and developing brain, retina, and epidermis through a M-CSF receptor-dependent
1064 invasive process. Dev. Biol. *238*. https://doi.org/10.1006/dbio.2001.0393.

1065 60. Ellett, F., Pase, L., Hayman, J.W., Andrianopoulos, A., and Lieschke, G.J. (2011). mpeg1 promoter
1066 transgenes direct macrophage-lineage expression in zebrafish. Blood *117*, e49–e56.

1067 61. Ranawat, N., and Masai, I. (2021). Mechanisms underlying microglial colonization of developing
1068 neural retina in zebrafish. Elife *10*. https://doi.org/10.7554/eLife.70550.

1069 62. Mazzolini, J., Le Clerc, S., Morisse, G., Coulonges, C., Kuil, L.E., van Ham, T.J., Zagury, J.-F., and
1070 Sieger, D. (2020). Gene expression profiling reveals a conserved microglia signature in larval
1071 zebrafish. Glia *68*, 298–315.

1072 63. Woodburn, S.C., Bollinger, J.L., and Wohleb, E.S. (2021). The semantics of microglia activation:
1073 neuroinflammation, homeostasis, and stress. J. Neuroinflammation *18*, 1–16.

1074 64. Stopper, L., Bălşeanu, T.A., Cătălin, B., Rogoveanu, O.C., Mogoantă, L., and Scheller, A. (2018).
1075 Microglia morphology in the physiological and diseased brain - from fixed tissue to in vivo
1076 conditions. Rom. J. Morphol. Embryol. *59*, 7–12.

1077 65. Marsh, S.E., Walker, A.J., Kamath, T., Dissing-Olesen, L., Hammond, T.R., de Soysa, T.Y., Young,
1078 A.M.H., Murphy, S., Abdulraouf, A., Nadaf, N., et al. (2022). Dissection of artifactual and
1079 confounding glial signatures by single-cell sequencing of mouse and human brain. Nat. Neurosci. *25*,
1080 306–316.

1081 66. Ma, S., Skarica, M., Li, Q., Xu, C., Risgaard, R.D., Tebbenkamp, A.T.N., Mato-Blanco, X., Kovner,
1082 R., Krsnik, Ž., de Martin, X., et al. (2022). Molecular and cellular evolution of the primate
1083 dorsolateral prefrontal cortex. Science. https://doi.org/10.1126/science.abo7257.

1084 67. Zhang, Y., and Beachy, P.A. (2023). Cellular and molecular mechanisms of Hedgehog signalling.
1085 Nat. Rev. Mol. Cell Biol. *24*, 668–687.

1086 68. Cowan, C.S., Renner, M., De Gennaro, M., Gross-Scherf, B., Goldblum, D., Hou, Y., Munz, M.,
1087 Rodrigues, T.M., Krol, J., Szikra, T., et al. (2020). Cell Types of the Human Retina and Its
1088 Organoids at Single-Cell Resolution. Cell *182*. https://doi.org/10.1016/j.cell.2020.08.013.

1089 69. Jacobo Lopez, A., Kim, S., Qian, X., Rogers, J., Stout, J.T., Thomasy, S.M., La Torre, A., Chen, R.,
1090 and Moshiri, A. (2022). Retinal organoids derived from rhesus macaque iPSCs undergo accelerated
1091 differentiation compared to human stem cells. Cell Prolif. *55*, e13198.

1092 70. Hahn, J., Monavarfeshani, A., Qiao, M., Kao, A.H., Kölsch, Y., Kumar, A., Kunze, V.P., Rasys,
1093 A.M., Richardson, R., Wekselblatt, J.B., et al. (2023). Evolution of neuronal cell classes and types in
1094 the vertebrate retina. Nature *624*, 415–424.

1095 71. Peng, Y.-R., Shekhar, K., Yan, W., Herrmann, D., Sappington, A., Bryman, G.S., van Zyl, T., Do,
1096 M.T.H., Regev, A., and Sanes, J.R. (2019). Molecular Classification and Comparative Taxonomics
1097 of Foveal and Peripheral Cells in Primate Retina. Cell *176*, 1222–1237.e22.

1098 72. Lee, B.B., Martin, P.R., and Grünert, U. (2010). Retinal connectivity and primate vision. Prog.
1099 Retin. Eye Res. *29*. https://doi.org/10.1016/j.preteyeres.2010.08.004.

1100 73. LeFauve, M.K., Rowe, C.J., Crowley-Perry, M., Wiegand, J.L., Shapiro, A.G., and Connaughton,
1101 V.P. (2021). Using a variant of the optomotor response as a visual defect detection assay in
1102 zebrafish. J Biol Methods *8*, e144.

1103 74. Emran, F., Rihel, J., Adolph, A.R., and Dowling, J.E. (2010). Zebrafish larvae lose vision at night.
1104 Proc. Natl. Acad. Sci. U. S. A. *107*, 6034–6039.

1105 75. Emran, F., Rihel, J., and Dowling, J.E. (2008). A behavioral assay to measure responsiveness of
1106 zebrafish to changes in light intensities. J. Vis. Exp. https://doi.org/10.3791/923.

1107 76. Kist, A.M., and Portugues, R. (2019). Optomotor Swimming in Larval Zebrafish Is Driven by Global
1108 Whole-Field Visual Motion and Local Light-Dark Transitions. Cell Rep. *29*, 659–670.e3.

1109 77. Neuhauss, S.C., Biehlmaier, O., Seeliger, M.W., Das, T., Kohler, K., Harris, W.A., and Baier, H.
1110 (1999). Genetic disorders of vision revealed by a behavioral screen of 400 essential loci in zebrafish.
1111 J. Neurosci. *19*, 8603–8615.

1112 78. Blockus, H., and Chédotal, A. (2016). Slit-Robo signaling. Development *143*, 3037–3044.

1113 79. Ordan, E., and Volk, T. (2015). Cleaved Slit directs embryonic muscles. Fly *9*, 82–85.

1114 80. Chen, S., Francioli, L.C., Goodrich, J.K., Collins, R.L., Kanai, M., Wang, Q., Alföldi, J., Watts,
1115 N.A., Vittal, C., Gauthier, L.D., et al. (2023). A genomic mutational constraint map using variation
1116 in 76,156 human genomes. Nature *625*, 92–100.

1117 81. El-Brolosy, M.A., Kontarakis, Z., Rossi, A., Kuenne, C., Günther, S., Fukuda, N., Kikhi, K., Boezio,
1118 G.L.M., Takacs, C.M., Lai, S.-L., et al. (2019). Genetic compensation triggered by mutant mRNA
1119 degradation. Nature *568*, 193–197.

1120 82. Lesca, G., Rudolf, G., Bruneau, N., Lozovaya, N., Labalme, A., Boutry-Kryza, N., Salmi, M.,
1121 Tsintsadze, T., Addis, L., Motte, J., et al. (2013). GRIN2A mutations in acquired epileptic aphasia
1122 and related childhood focal epilepsies and encephalopathies with speech and language dysfunction.
1123 Nat. Genet. *45*, 1061–1066.

1124 83. Diaz-Salazar, C., Krzisch, M., Yoo, J., Nano, P.R., Bhaduri, A., Jaenisch, R., and Polleux, F. (2024).
1125 Human-specific paralogs of SRGAP2 induce neotenic features of microglia structural and functional
1126 maturation. bioRxiv. https://doi.org/10.1101/2024.06.28.601266.

1127 84. Bacon, C., Endris, V., and Rappold, G. (2009). Dynamic expression of the Slit-Robo GTPase
1128 activating protein genes during development of the murine nervous system. J. Comp. Neurol. *513*,
1129 224–236.

1130 85. Slingsby, C., and Wistow, G.J. (2014). Functions of crystallins in and out of lens: roles in elongated
1131 and post-mitotic cells. Prog. Biophys. Mol. Biol. *115*, 52–67.

1132 86. Shao, W.-Y., Liu, X., Gu, X.-L., Ying, X., Wu, N., Xu, H.-W., and Wang, Y. (2016). Promotion of
1133 axon regeneration and inhibition of astrocyte activation by alpha A-crystallin on crushed optic nerve.
1134 Int. J. Ophthalmol. *9*, 955.

1135 87. Burger, C.A., Jiang, D., Mackin, R.D., and Samuel, M.A. (2021). Development and maintenance of
1136 vision's first synapse. Dev. Biol. *476*. https://doi.org/10.1016/j.ydbio.2021.04.001.

1137 88. Neuhauss, S.C.F. (2003). Behavioral genetic approaches to visual system development and function
1138 in zebrafish. J. Neurobiol. *54*, 148–160.

1139 89. Thion, M.S., and Garel, S. (2017). On place and time: microglia in embryonic and perinatal brain
1140 development. Curr. Opin. Neurobiol. *47*, 121–130.

1141 90. Li, Q., and Barres, B.A. (2017). Microglia and macrophages in brain homeostasis and disease. Nat.
1142 Rev. Immunol. *18*, 225–242.

1143 91. Pascual, O., Ben Achour, S., Rostaing, P., Triller, A., and Bessis, A. (2012). Microglia activation
1144 triggers astrocyte-mediated modulation of excitatory neurotransmission. Proc. Natl. Acad. Sci. U. S.
1145 A. *109*, E197–E205.

1146 92. Yu, C., Deng, X.-J., and Xu, D. (2023). Microglia in epilepsy. Neurobiol. Dis. *185*, 106249.

1147 93. Veenstra-VanderWeele, J., O'Reilly, K.C., Dennis, M.Y., Uribe-Salazar, J.M., and Amaral, D.G.
1148 (2023). Translational Neuroscience Approaches to Understanding Autism. Am. J. Psychiatry *180*,
1149 265–276.

1150 94. Rea, V., and Van Raay, T.J. (2020). Using Zebrafish to Model Autism Spectrum Disorder: A
1151 Comparison of ASD Risk Genes Between Zebrafish and Their Mammalian Counterparts. Front.
1152 Mol. Neurosci. *13*, 575575.

1153 95. Tayanloo-Beik, A., Hamidpour, S.K., Abedi, M., Shojaei, H., Tavirani, M.R., Namazi, N., Larijani,
1154 B., and Arjmand, B. (2022). Zebrafish Modeling of Autism Spectrum Disorders, Current Status and
1155 Future Prospective. Front. Psychiatry *13*, 911770.

1156 96. Modeling autism spectrum disorders in zebrafish (2020). In Behavioral and Neural Genetics of
1157 Zebrafish (Academic Press), pp. 451–480.

1158 97. Sakai, C., Ijaz, S., and Hoffman, E.J. (2018). Zebrafish Models of Neurodevelopmental Disorders:
1159 Past, Present, and Future. Front. Mol. Neurosci. *11*, 294.

1160 98. Costa, F.V., Zabegalov, K.N., Kolesnikova, T.O., de Abreu, M.S., Kotova, M.M., Petersen, E.V.,
1161 and Kalueff, A.V. (2023). Experimental models of human cortical malformations: from mammals to
1162 "acortical" zebrafish. Neurosci. Biobehav. Rev. *155*, 105429.

1163 99. LaFave, M.C., Varshney, G.K., Vemulapalli, M., Mullikin, J.C., and Burgess, S.M. (2014). A
1164 defined zebrafish line for high-throughput genetics and genomics: NHGRI-1. Genetics *198*, 167–
1165 170.

1166 100. Westerfield, M. (1995). The Zebrafish Book: A Guide for the Laboratory Use of Zebrafish (Danio
1167 Rerio).

1168 101. Zerbino, D.R., Achuthan, P., Akanni, W., Ridwan Amode, M., Barrell, D., Bhai, J., Billis, K.,
1169 Cummins, C., Gall, A., Girón, C.G., et al. (2018). Ensembl 2018. Preprint,
1170 https://doi.org/10.1093/nar/gkx1098 https://doi.org/10.1093/nar/gkx1098.

1171 102. UniProt Consortium (2019). UniProt: a worldwide hub of protein knowledge. Nucleic Acids Res. *47*,
1172 D506–D515.

1173 103. National Center for Biotechnology Information (Verenigde Staten). (2002). The NCBI Handbook.

1174 104. Rothbauer, U., Zolghadr, K., Muyldermans, S., Schepers, A., Cardoso, M.C., and Leonhardt, H.
1175 (2008). A versatile nanotrap for biochemical and functional studies with fluorescent fusion proteins.

1176 Mol. Cell. Proteomics *7*, 282–289.

1177 105. Andrews, S., and Others (2010). FastQC: a quality control tool for high throughput sequence data.
1178 Preprint at Babraham Bioinformatics, Babraham Institute, Cambridge, United Kingdom.

1179 106. Bolger, A.M., Lohse, M., and Usadel, B. (2014). Trimmomatic: a flexible trimmer for Illumina
1180 sequence data. Bioinformatics *30*, 2114–2120.

1181 107. Patro, R., Duggal, G., Love, M.I., Irizarry, R.A., and Kingsford, C. (2017). Salmon provides fast and
1182 bias-aware quantification of transcript expression. Nat. Methods *14*, 417–419.

1183 108. Thisse, C., and Thisse, B. (2008). High-resolution in situ hybridization to whole-mount zebrafish
1184 embryos. Nat. Protoc. *3*, 59–69.

1185 109. Jao, L.-E., Wente, S.R., and Chen, W. (2013). Efficient multiplex biallelic zebrafish genome editing
1186 using a CRISPR nuclease system. Proc. Natl. Acad. Sci. U. S. A. *110*, 13904–13909.

1187 110. Jao, L.-E., Appel, B., and Wente, S.R. (2012). A zebrafish model of lethal congenital contracture
1188 syndrome 1 reveals Gle1 function in spinal neural precursor survival and motor axon arborization.
1189 Development *139*, 1316–1326.

1190 111. Moreno-Mateos, M.A., Vejnar, C.E., Beaudoin, J.-D., Fernandez, J.P., Mis, E.K., Khokha, M.K.,
1191 and Giraldez, A.J. (2015). CRISPRscan: designing highly efficient sgRNAs for CRISPR-Cas9
1192 targeting in vivo. Nat. Methods *12*, 982–988.

1193 112. Lindsay, H., Burger, A., Biyong, B., Felker, A., Hess, C., Zaugg, J., Chiavacci, E., Anders, C., Jinek,
1194 M., Mosimann, C., et al. (2016). CrispRVariants charts the mutation spectrum of genome
1195 engineering experiments. Nat. Biotechnol. *34*, 701–702.

1196 113. Colón-Rodríguez, A., Uribe-Salazar, J.M., Weyenberg, K.B., Sriram, A., Quezada, A., Kaya, G.,
1197 Jao, E., Radke, B., Lein, P.J., and Dennis, M.Y. (2020). Assessment of Autism Zebrafish Mutant
1198 Models Using a High-Throughput Larval Phenotyping Platform. Front Cell Dev Biol *8*, 586296.

1199 114. Tsai, S.Q., Nguyen, N.T., Malagon-Lopez, J., Topkar, V.V., Aryee, M.J., and Joung, J.K. (2017).
1200 CIRCLE-seq: a highly sensitive in vitro screen for genome-wide CRISPR-Cas9 nuclease off-targets.
1201 Nat. Methods *14*, 607–614.

1202 115. Lazzarotto, C.R., Nguyen, N.T., Tang, X., Malagon-Lopez, J., Guo, J.A., Aryee, M.J., Joung, J.K.,
1203 and Tsai, S.Q. (2018). Defining CRISPR-Cas9 genome-wide nuclease activities with CIRCLE-seq.
1204 Nat. Protoc. *13*, 2615–2642.

1205 116. Shafik, A.M., and Cifuentes, D. (2018). Zebrafish as a Tool to Study Congenital Heart Diseases.
1206 Preprint, https://doi.org/10.1016/b978-0-12-809657-4.64146-7 https://doi.org/10.1016/b978-0-12-
1207 809657-4.64146-7.

1208 117. Kretov, D.A., Shafik, A.M., and Cifuentes, D. (2018). Assessing miR-451 Activity and Its Role in
1209 Erythropoiesis. Methods Mol. Biol. *1680*, 179–190.

1210 118. Pulak, R. (2016). Tools for automating the imaging of zebrafish larvae. Methods *96*, 118–126.

1211 119. Teixidó, E., Kießling, T.R., Krupp, E., Quevedo, C., Muriana, A., and Scholz, S. (2019). Automated
1212 Morphological Feature Assessment for Zebrafish Embryo Developmental Toxicity Screens. Toxicol.
1213 Sci. *167*, 438–449.

1214 120. Lawson, N.D., Li, R., Shin, M., Grosse, A., Yukselen, O., Stone, O.A., Kucukural, A., and Zhu, L.

1215 (2020). An improved zebrafish transcriptome annotation for sensitive and comprehensive detection
1216 of cell type-specific genes. https://doi.org/10.7554/eLife.55792.

1217 121. Dobin, A., Davis, C.A., Schlesinger, F., Drenkow, J., Zaleski, C., Jha, S., Batut, P., Chaisson, M.,
1218 and Gingeras, T.R. (2013). STAR: ultrafast universal RNA-seq aligner. Preprint,
1219 https://doi.org/10.1093/bioinformatics/bts635 https://doi.org/10.1093/bioinformatics/bts635.

1220 122. Putri, G.H., Anders, S., Pyl, P.T., Pimanda, J.E., and Zanini, F. (2022). Analysing high-throughput
1221 sequencing data in Python with HTSeq 2.0. Bioinformatics *38*, 2943–2945.

1222 123. Love, M.I., Huber, W., and Anders, S. (2014). Moderated estimation of fold change and dispersion
1223 for RNA-seq data with DESeq2. Genome Biol. *15*, 550.

1224 124. Yu, G., Wang, L.-G., Han, Y., and He, Q.-Y. (2012). clusterProfiler: an R package for comparing
1225 biological themes among gene clusters. OMICS *16*, 284–287.

1226 125. Farnsworth, D.R., Saunders, L.M., and Miller, A.C. (2020). A single-cell transcriptome atlas for
1227 zebrafish development. Dev. Biol. *459*, 100–108.

1228 126. Bresciani, E., Broadbridge, E., and Liu, P.P. (2018). An efficient dissociation protocol for generation
1229 of single cell suspension from zebrafish embryos and larvae. MethodsX *5*, 1287–1290.

1230 127. Hao, Y., Hao, S., Andersen-Nissen, E., Mauck, W.M., 3rd, Zheng, S., Butler, A., Lee, M.J., Wilk,
1231 A.J., Darby, C., Zager, M., et al. (2021). Integrated analysis of multimodal single-cell data. Cell *184*,
1232 3573–3587.e29.

1233 128. McGinnis, C.S., Murrow, L.M., and Gartner, Z.J. (2019). DoubletFinder: Doublet Detection in
1234 Single-Cell RNA Sequencing Data Using Artificial Nearest Neighbors. Cell systems *8*, 329.

1235 129. Tran, V., Papalexi, E., Schroeder, S., Kim, G., Sapre, A., Pangallo, J., Sova, A., Matulich, P.,
1236 Kenyon, L., Sayar, Z., et al. (2022). High sensitivity single cell RNA sequencing with split pool
1237 barcoding. bioRxiv, 2022.08.27.505512. https://doi.org/10.1101/2022.08.27.505512.

1238 130. Bradford, Y.M., Van Slyke, C.E., Ruzicka, L., Singer, A., Eagle, A., Fashena, D., Howe, D.G.,
1239 Frazer, K., Martin, R., Paddock, H., et al. (2022). Zebrafish information network, the knowledgebase
1240 for Danio rerio research. Genetics *220*. https://doi.org/10.1093/genetics/iyac016.

1241 131. Finak, G., McDavid, A., Yajima, M., Deng, J., Gersuk, V., Shalek, A.K., Slichter, C.K., Miller,
1242 H.W., Juliana McElrath, M., Prlic, M., et al. (2015). MAST: a flexible statistical framework for
1243 assessing transcriptional changes and characterizing heterogeneity in single-cell RNA sequencing
1244 data. Genome Biol. *16*. https://doi.org/10.1186/s13059-015-0844-5.

1245 132. Marsh, S.E., Salmon, M., and Hoffman, P. scCustomize: custom visualizations & functions for
1246 streamlined analyses of single cell sequencing. Preprint at https://doi. org/10.5281/zenodo.

1247 133. Schindelin, J., Arganda-Carreras, I., Frise, E., Kaynig, V., Longair, M., Pietzsch, T., Preibisch, S.,
1248 Rueden, C., Saalfeld, S., Schmid, B., et al. (2012). Fiji: an open-source platform for biological-image
1249 analysis. Nat. Methods *9*, 676–682.

1250 134. Silva, N.J., Dorman, L.C., Vainchtein, I.D., Horneck, N.C., and Molofsky, A.V. (2021). In situ and
1251 transcriptomic identification of microglia in synapse-rich regions of the developing zebrafish brain.
1252 Nat. Commun. *12*, 5916.

1253 135. Shiau, C.E., Monk, K.R., Joo, W., and Talbot, W.S. (2013). An anti-inflammatory NOD-like

1254 receptor is required for microglia development. Cell Rep. *5*, 1342–1352.

1255 136. Welch, J.D., Kozareva, V., Ferreira, A., Vanderburg, C., Martin, C., and Macosko, E.Z. (2019).
1256 Single-Cell Multi-omic Integration Compares and Contrasts Features of Brain Cell Identity. Cell
1257 *177*, 1873–1887.e17.

1258 137. Jorstad, N.L., Song, J.H.T., Exposito-Alonso, D., Suresh, H., Castro-Pacheco, N., Krienen, F.M.,
1259 Yanny, A.M., Close, J., Gelfand, E., Long, B., et al. (2023). Comparative transcriptomics reveals
1260 human-specific cortical features. Science. https://doi.org/10.1126/science.ade9516.

1261 138. Sherman, B.T., Hao, M., Qiu, J., Jiao, X., Baseler, M.W., Lane, H.C., Imamichi, T., and Chang, W.
1262 (2022). DAVID: a web server for functional enrichment analysis and functional annotation of gene
1263 lists (2021 update). Nucleic Acids Res. *50*. https://doi.org/10.1093/nar/gkac194.